Research Square

Preprints are preliminary reports that have not undergone peer review.
They should not be considered conclusive, used to inform clinical practice,
or referenced by the media as validated information.

Ligand-regulated ACKR3 nanoclustering shapes CXCR4 signaling at the plasma membrane

Noelia Santander-Acerete
Centro Nacional de Biotecnologia
Eva Mª García-Cuesta
Centro Nacional de Biotecnologia
Sofía R. Gardeta
Centro Nacional de Biotecnologia
Ricardo Villares
Centro Nacional de Biotecnologia
Marc Artinger
University of Constance: Universitat Konstanz
Oliver J Gerken
University of Konstanz: Universitat Konstanz
Rosa Ayala Bueno
Centro Nacional de Biotecnologia
Rob Leurs
Vrije Universiteit Amsterdam
Henry F Vischer
Vrije Universiteit Amsterdam
Ana Cayuela
CNIO: Centro Nacional de Investigaciones Oncologicas
Nicolás Mateos
ICFO: Institut de Ciencies Fotoniques
Blanca Soler Palacios
CNB: Centro Nacional de Biotecnologia
José Miguel Rodríguez-Frade
CNB: Centro Nacional de Biotecnologia
Daniel F Legler
University of Konstanz: Universitat Konstanz
Mario Mellado
mmellado@cnb.csic.es

CNB: Centro Nacional de Biotecnologia https://orcid.org/0000-0001-6325-1630

Research Article

Keywords:

Posted Date: July 20th, 2026

DOI: https://doi.org/10.21203/rs.3.rs-10307977/v1

License: This work is licensed under a Creative Commons Attribution 4.0 International License.
Read Full License

Ligand-regulated ACKR3 nanoclustering shapes CXCR4 signaling at the plasma membrane

Noelia Santander Acerete[1], Eva Mª García-Cuesta[1], Sofía R Gardeta[1], Ricardo Villares[1], Marc Artinger[2], Oliver J. Gerken[2], Rosa Ayala Bueno[1], Rob Leurs[3], Henry F. Vischer[3], Ana Cayuela[4], Nicolas Mateos[5], Blanca Soler Palacios[1], José Miguel-Rodríguez-Frade[1], Daniel F. Legler[2,6,7], and Mario Mellado[1*]

[1] Laboratory of Chemokine receptor signaling, Department of Immunology and Oncology, Centro Nacional de Biotecnología/CSIC, 28049-Madrid, Spain

[2] Institute of Cell Biology and Immunology Thurgau (BITG), at the University of Konstanz, Kreuzlingen, Switzerland

[3] Division of Medicinal Chemistry, Faculty of Science, Amsterdam Institute of Molecular and Life Sciences, Vrije Universiteit Amsterdam, 1081 HV Amsterdam, The Netherlands

[4] Confocal Microscopy Unit, Centro Nacional de Investigaciones Oncologicas, 28029-Madrid, Spain

[5] Super resolution Light microscopy and Nanoscopy (SLN) facility, ICFO - Institut de Ciencies Fotoniques, The Barcelona Institute of Science and Technology, Castelldefels 08860-Barcelona, Spain

[6] Faculty of Biology, University of Konstanz, Konstanz, Germany

[7] Theodor Kocher Institute, University of Bern, Bern, Switzerland

[*]Corresponding author:

Mario Mellado

mmellado@cnb.csic.es

Tfno. +34 915854852

Fax: (+34) 913720493

Funding

This work was supported in part by The Spanish National Plan for Scientific and Technical Research and Innovation (PDI2023-146301OB.I00 to M.M.) and the Fundación para el Conocimiento Madri+d (CAM22/BMD-7274 to M.M.); the Swiss National Science Foundation (SNSF grant # 220205 to D.F.L.), the Thurgauische Stiftung für Wissenschaft und Forschung (D.F.L.), and the State Secretariat for Education, Research and Innovation (D.F.L.). D.F.L. is supported by the Irène and Max Gsell Foundation (IMGS). EMG-C and R.V. are supported by the Severo Ochoa Award (CEX2023-001386-S, Spanish Ministry of Science, University and Innovation); NSA and SRG are supported by the Spanish National Plan for Scientific and Technical Research and Innovation (PRE2021-098903- and PRE2018-083201, respectively). BS and R.A-B are supported by the Fundación para el Conocimiento Madri+d (CAM22/BMD-7274). The funders had no role in the study design, data collection and analysis, decision to publish, or preparation of the manuscript.

Abstract

Recent advances in imaging have revealed that chemokine receptors integrate extracellular cues *via* dynamic nanoscale organization at the plasma membrane. While the atypical chemokine receptor ACKR3 is a known regulator of chemokine availability, its spatial organization and specific signaling contributions remain poorly defined. In this study, we employed single-particle tracking and quantitative total internal reflection fluorescence microscopy to characterize the spatio-temporal distribution and molecular dynamics of ACKR3 on T cells. We further investigated its interplay with the canonical chemokine receptor CXCR4. Our results demonstrate that ACKR3 exists as a mixture of monomers, dimers, and higher-order nanoclusters, the formation of which is driven by ligand binding. Stimulation with CXCL12 or the ACKR3-selective small molecule agonist VUF15485 induces robust ACKR3 oligomerization independent of CXCR4 expression, G-protein coupling, β-arrestin recruitment, or actin cytoskeleton remodeling. Dual-color single-molecule imaging further reveals dynamic CXCR4/ACKR3 heterocomplexes that are modulated by CXCL12. Functionally, ACKR3 co-expression attenuates CXCL12-induced CXCR4–$G\alpha_i$ signaling and subsequent cAMP inhibition. Together, these findings identify ACKR3 as an active organizer of chemokine receptor nanoscale architecture, providing a mechanistic framework for how ACKR3 fine-tunes CXCR4 signaling beyond its established role as a chemokine scavenger.

Keywords

Chemokines, receptors, oligomers, signaling, immune T cells

Introduction

Chemokines are a family of chemotactic cytokines that regulate essential cellular processes, including migration, proliferation, survival, differentiation, and cytokine release. They exert their biological effects by binding to specific G-protein coupled receptors (GPCRs), which typically signal through heterotrimeric G-proteins and β-arrestin pathways. In humans, the chemokine system comprises 23 receptors, classified according to the specific chemokine subfamilies they bind [1]. However, a subset of structurally homologous receptors exists that do not initiate classical Gi-protein-mediated signaling [2]. These are termed atypical chemokine receptors (ACKRs) [3], and are characterized by the absence or mutation of the canonical DRYLAIV motif, a sequence located in the second intracellular loop strictly required for G-protein binding and activation [4, 5]. To date, five ACKRs have been identified: ACKR1/DARC, ACKR2/D6, ACKR3/CXCR7, ACKR4/CCRL1, and ACKR5/GPR182 [6, 7]. While ACKRs were initially considered "silent" receptors primarily involved in regulating extracellular chemokine bioavailability [8], emerging evidence indicates that, with the exception of ACKR1 [9], they also modulate chemokine functions by triggering β-arrestin recruitment. In some cases, this recruitment is associated with tuning receptor dynamics at both intracellular and extracellular regions [10]. Although the association of β-arrestins with ACKR3 is well-documented [9], the functional differences between β-arrestin1 and β-arrestin2 recruitment have not been fully elucidated [11]. Furthermore, ACKRs can form heterodimers with classical chemokine receptors to modulate their biological functions [12, 13]. For example, ACKR3 regulates CXCL12-mediated T-cell chemotaxis both by sequestering the ligand and by directly modulating CXCR4-mediated G-protein activation through physical association [13].

ACKR3, also known as RDC1 or CXCR7, is a multi-ligand atypical chemokine receptor that binds CXCL12 [14] , CXCL11 [14], vCCL2 [15], as well as several opioid-derived peptides [16, 17]. Although originally classified as a non-signaling "decoy" receptor, ACKR3 is essential for survival. Similar to CXCR4 [12, 18, 19], ACKR3-deficient mice exhibit perinatal lethality due to severe cardiac development defects and lymphatic vessel hyperplasia [20]. Within the immune system, ACKR3 is expressed intracellularly in T cells and monocytes [21] and on the plasma membrane of B cells, plasmacytoid dendritic cells, natural killer cells, and basophils [22]. Additionally, some reports have shown reduced but functionally active expression of ACKR3 on the surface of T cells, suggesting that the intracellular pool of ACKR3 undergoes constitutive trafficking to the cell membrane to facilitate signaling [23, 24]. A primary function of ACKR3 is the modulation of the CXCL12/CXCR4 signaling axis [25]. By continuously cycling

between the plasma membrane and intracellular compartments [26], ACKR3 regulates extracellular chemokine availability and subsequent CXCR4 signaling dynamics. This regulatory process is driven by the phosphorylation of the ACKR3 C-terminus by GPCR kinases (GRKs), which facilitates β-arrestin recruitment [27]. These responses are further potentiated by the formation and stabilization of CXCR4/ACKR3 heterocomplexes [12, 28].

Recent evidence suggests that large-scale molecular assemblies, or signaling nanoclusters, at the plasma membrane, serve as critical regulators of cellular function [29]. Such spatial organization has been characterized for various transmembrane receptors, including neurotransmitter [30] and immune [31, 32] receptors. For example, CD4 is organized into pre-existing clusters that expand upon T-cell activation, thereby modulating the magnitude of downstream signaling [33, 34]. Similarly, CXCR4 is distributed at the cell surface as a mixture of monomers, dimers, and small oligomers (≥3 receptors). CXCL12 binding shifts this equilibrium, decreasing the monomeric and dimeric populations while promoting the formation of large CXCR4 nanoclusters. This reorganization alters receptor lateral mobility and spatial organization at the cell membrane [35], a process essential for the accurate sensing of chemoattractant gradients [35, 36].

In this study, we employed quantitative single-molecule spatio-dynamic imaging to elucidate the molecular organization and spatial distribution of ACKR3 at the plasma membrane. We specifically investigated how CXCL12 alters ACKR3 conformational dynamics and how co-expression of CXCR4, that shares the same ligand, modulates these dynamics. Our data indicate that CXCR4 facilitates the surface expression of ACKR3 in T cells. Furthermore, ACKR3 activation by either CXCL12 or the selective synthetic agonist VUF15485 promotes receptor oligomerization independently of CXCR4 presence. Notably, the mechanism of ACKR3 oligomerization diverges significantly from that of CXCR4; while CXCR4 clustering requires β-arrestin1 recruitment and dynamic actin cytoskeleton remodeling, ACKR3 oligomerization occurs independently of β-arrestin coupling and activation. In cells co-expressing both receptors, we identified a population of CXCR4/ACKR3 heterocomplexes that increases upon CXCL12 stimulation. These heterocomplexes co-diffuse within the plasma membrane and coexist alongside discrete CXCR4 and ACKR3 oligomers.

These findings highlight the sophisticated dynamics of chemokine receptors and their broader influence on cellular signaling. Ligand-induced receptor oligomerization is not exclusive to canonical receptors such as CXCR4 but is a shared feature with atypical chemokine receptors. The detection of surface

CXCR4/ACKR3 heterocomplexes suggests that, beyond regulating ligand bioavailability, ACKR3 serves as a functional modulator that fine-tunes CXCR4-mediated responses. What was once viewed as a simple signaling system has evolved into a highly complex molecular machinery; understanding this architecture provides a mechanistic framework that may reveal promising new opportunities for drug discovery.

Materials and methods

Cells and reagents

HEK-293 cells and Jurkat (JK) human leukemia cells were obtained from the American Type Culture Collection (CRL-3216 and CRL-10915, respectively; ATCC, Rockville, MD). The generation and characterization of JKX4$^{-/-}$ and JKX4$^{-/-}$β1$^{-/-}$ cells have been previously described [36]. Jurkat X4-AcGFP knock-in cells (JKX4-AcGFP-KI) were a kind gift from Dr. Laura Martínez Muñoz, (CABIMER, University of Seville, Spain).

Human CXCL12 was purchased from PeproTech (Rocky Hill, NJ). The ACKR3-selective small molecule agonist VUF15485[37] and its antagonist VUF16840[38] were kind gifts from Drs. Rob Leurs and Henry F. Vischer (Vrije Universiteit, Amsterdam, The Netherlands). The following antibodies were used: anti-human CXCR4 monoclonal antibody (mAb) (clone 44717), PE-conjugated anti-human CXCR4 mAb (clone 12G5), and anti-human ACKR3 mAb (clone 11G8) (all from R&D Systems, Minneapolis, MN); BV421-conjugated anti-human CXCR4 mAb (clone 12G5) (#306518), and BV421-conjugated mouse IgG2a,κ isotype control antibody (#400259; all from Biolegend, San Diego, CA); APC-conjugated anti-human ACKR3 mAb (clone 11G8) (R&D Systems; #FAB4227A-025), APC-conjugated anti-human IgG Fc antibody (R&D Systems; #FAB110A); goat F(ab')2 anti-mouse IgG-PE (Southern Biotech, Birmingham, AL); Alexa Fluor™ 488-conjugated goat anti-mouse IgG (H+L) cross-adsorbed secondary antibody (ThermoFisher Scientific, Waltham, MA; AB_2534069); anti-human β-arrestin 1/2 (D24H9) mAb (#4674, Cell Signaling Technology, Danvers, MA); hFAb anti-tubulin antibody (#64554219, Bio-Rad, Hercules, CA); and anti-ICAM-3 mAb (clone HP2/19), kindly donated by Dr. Francisco Sánchez Madrid (Health Institute La Princesa Hospital, Madrid, Spain). We also used phalloidin-TRITC (#P1951, Sigma-Merck, St Louis, MO), pertussis toxin (Sigma-Aldrich), the luciferase substrate coelenterazine H (Biosynth AG, Staad, Switzerland), and the fluorophore SNAP-Cell TMR Star (New England Biolabs [NEB], Ipswich, MA).

Recombinant DNA plasmids

The ACKR3ΔCt mutant was generated using the pcDNA.3-ACKR3 expression vector as a PCR template. The insert was amplified with Taq DNA Polymerase High Fidelity (ThermoFisher) using 5'HindIII (5'TATAAGCTTCATTACGATGGATCTGC3') and 3'BamHI (5'TATGGATCCCCATTGATGAAGCT GTAGA3') primers, and subsequently cloned into the pcDNA.3-AcGFP expression vector. The pcDNA.3-AcGFP backbone was obtained from pcDNA.3-ACKR3-AcGFP by digestion with HindIII (NEB, #R0104S) and BamHI (NEB, #R0136S). Successful cloning of pcDNA.3-ACKR3ΔCt-AcGFP was confirmed by DNA sequencing.

To generate the pSNAPf-ACKR3-SNAP-tag plasmid, we used pECFP-ACKR3 as the template. The insert was amplified by PCR using 5'NheI (5'AAAGCTAGCATGGATCTGCATCTCT 3') and 3'EcoRI (5' TTTGAATTCTTTGGTGCTCTGCTC 3') primers and then cloned into the pSNAPf vector (NEB) using NheI (NEB, #R0131S) and EcoRI (NEB, #R0101S). Correct construction of the pSNAPf-ACKR3-SNAP-tag plasmid was confirmed by DNA sequencing.

CRISPR-Cas9 gene editing

To generate JK cells lacking ACKR3 (JKA3$^{-/-}$), and cells lacking β-arrestins 1 and 2 (JKX4$^{-/-}$β1$^{-/-}$β2$^{-/-}$), single-guide RNAs (sgRNAs; Table I) targeting *ACKR3* and *β-arrestin2* were cloned into the pSpCas9(BB)-2A-GFP plasmid (PX458; Addgene, Cambridge, MA). This construct allows Cas9-mediated targeting of the genomic sequence of interest and GFP expression for selection. JK and JKX4$^{-/-}$β1$^{-/-}$ cells (2 × 10^7) were mixed with 20 μg of the corresponding plasmid DNA and electroporated at 280 V, using a single exponential pulse in 4-mm cuvettes (GenePulser Xcell^{TM}, Bio-Rad). Following electroporation, cells were cultured (24 h, 37ºC, 5% CO_2), in RPMI-1640 medium supplemented with 10% fetal calf serum (FCS), and GFP$^+$ cells were then sorted and seeded into 96-well plates (1 cell/well) containing RPMI-1640 supplemented with 10% FCS and 1% penicillin/streptomycin. Single-cell clones were expanded and screened for genomic bi-allelic modifications by PCR and nanopore sequencing (Table I). Loss of β-arrestin2 protein expression was further confirmed by western blotting (Supplementary Fig. 1). Loss of ACKR3 was confirmed by immune staining with anti-ACKR3 mAb (clone 11G8) followed by anti-mouse IgG-Alexa Fluor 488 (green) (Supplementary Fig. 2A, B), and by 2% agarose gel size-based separation of PCR products (Supplementary Fig. 2C).

Transient transfection studies

Where indicated, JK, JKX4$^{-/-}$, JKA3$^{-/-}$, or JKX4$^{-/-}$β1$^{-/-}$β2$^{-/-}$ cells were transiently transfected with plasmids encoding CXCR4-AcGFP, ACKR3-AcGFP, or ACKR3ΔCt-AcGFP (20 μg), as described [36]. Briefly, 2 × 10^7 cells were mixed with 20 μg plasmid DNA and electroporated at 280 V, using a single exponential pulse in 4-mm cuvettes (GenePulser Xcell^{TM}). For dual total internal reflection fluorescence microscopy (TIRF-M) studies, JKX4-AcGFP-KI cells (2.5 × 10^6) were mixed with 10 μg of plasmid RNA encoding ACKR3-SNAP-tag and electroporated at 300 V, using a single 2 ms square-wave pulse in 2-mm cuvettes (GenePulser Xcell^{TM}). Following electroporation, cells were cultured for 24 hours (37ºC, 5% CO_2) in RPMI-1640 supplemented with 10% FCS before experiments were performed. When HEK-293 transfectants were required, transient transfections were performed using the Neon™ Transfection System (ThermoFisher). Briefly, 5 × 10^5 cells were mixed with 6 or 7.5 μg plasmid DNA and electroporated at 1,100 V, using two pulses of 20 ms duration. Cells were then maintained (24 h, 37ºC, 5% CO_2) in DMEM supplemented with 20% FCS until the experiments were conducted. Transfection efficiency in HEK-293 cells exceeded 95%.

Western blotting

A total of 3 × 10^6 cells were lysed in RIPA detergent buffer supplemented with 1 mM PMSF, 10 μg/mL aprotinin, 10 μg/mL leupeptin, and 10 μM sodium orthovanadate, for 30 minutes at 4ºC. Extracts were then analyzed by standard western blotting using specific antibodies.

Immunofluorescence analyses

Cells were attached onto fibronectin (20 μg/mL, Sigma-Aldrich)-coated glass slides. To study surface ACKR3 expression, cells were stimulated with 50 nM CXCL12 or buffer as a negative control at different time points (37°C), fixed with 4% paraformaldehyde (10 min, 4ºC), and blocked with PBS containing 150 mM NaCl, 0.1% goat serum, and 1% BSA (60 min, room temperature [RT]). Subsequently, cells were stained with an anti-ACKR3 mAb (11G8 clone) (30 min, RT) followed by an Alexa-Fluor 488 goat anti-mouse IgG (30 min, RT). Finally, cells were stained with an anti-transferrin receptor (TfR) antibody coupled to Alexa 647 (30 min, RT). For quantification, the corrected total cell fluorescence (CTCF) was calculated for each cell in the 488 nm and 638 nm channels using the same region of interest. In a second step, the values were normalized to the TfR signal, which was considered 100% membrane staining for each cell, using Fiji software (version 1.53).

To assess cell polarization, cells were stimulated with 100 nM CXCL12 (5 min at 37°C) or buffer as an unstimulated control, fixed with 4% paraformaldehyde (10 min, RT), and then blocked with PBS containing 150 mM NaCl, 0.1% goat serum, and 1% BSA (60 min, RT). Samples were then stained with an anti-human ICAM-3 mAb plus Alexa-Fluor 488 goat anti-mouse IgG (30 min, RT; ThermoFisher Scientific), permeabilized with 0.25% saponin (10 min, RT), and stained with phalloidin-TRITC (Sigma-Merck; 30 min, RT). Fluorescence imaging was performed using a Leica STELLARIS 5 multispectral confocal microscope (Wetzlar, Germany) equipped with a 63× oil-immersion objective, and quantified using Fiji (version 1.53).

cAMP determination

cAMP levels were determined using the cAMP-GloTM Max Assay (Promega, Madison, WI) in cells (5×10^5 cells/well) untreated or pretreated with CXCL12 (50 nM, 5 min, 37°C) followed by the addition of forskolin (10 μM, 10 min, 37°C).

Flow cytometry studies

Cells were incubated with specific antibodies (30 min, 4°C) and Geometric Mean fluorescence intensity was determined on a GALLIOS or Cytoflex flow cytometer (Beckman Coulter Inc., Brea, CA).

Actin polymerization was determined in cells (5×10^5 cells/well) activated with 50 nM CXCL12 or 1 μM VUF15485 at the indicated time points. Cells were fixed with 2% paraformaldehyde and permeabilized with 0.01% saponin, followed by Phalloidin-TRITC (30 min, RT) incubation, and analyzed in a Cytoflex cytometer (Beckman Coulter).

Proximity-based biochemical assays (Bystander NanoBiT and BRET assays)

Transfected HEK-293 cells were resuspended in PBS supplemented with 5 mM glucose and distributed in duplicate into a 96-well half-well plate (Perkin-Elmer, Waltham, MA). Coelenterazine H (5 μM) was then added to the cells, followed by incubation for 5 minutes at 37°C. For bystander NanoBit assays, baseline luminescence was measured every 30 seconds (385–440 nm, 350 ms integration time) for a further 5 minutes on a Tecan Spark 10 M multiplate reader (Tecan, Männdorf, Switzerland). Subsequently, cells were stimulated with the respective ligands or PBS as a negative control. The emitted luminescence was monitored every 30 seconds for an additional 15 minutes. For BRET assays, in addition to the

luminescence, recombinant GFP, rGFP, (490-560 nm, 350 ms integration time) or mVenus (505-590 nm, 350 ms integration time) fluorescence were measured every minute for 5 minutes before stimulation with the indicated ligands or PBS. Emitted luminescence and fluorescence were monitored for an additional 15 minutes. To calculate the BRET ratio, the fluorescence values were divided by the luminescence values.

For data analysis, the luminescence values or the BRET ratio from stimulated cells were normalized to those of unstimulated cells to determine the fold-change (ΔRLU/ΔBRET ratio), and the area under the curve (AUC) was determined for quantification.

Single-molecule TIRF imaging and analysis

Transfected cells expressing 8,500–22,000 receptors/cell (<4.5 particles/μm^2) were selected for detection and tracking analyses (Supplementary Fig. 3A). Experiments were performed at 37ºC and 5% CO_2 using a TIRF microscope (LeicaAM TIRF inverted microscope; Leica Microsystems) equipped with a Hamamatsu Flash 4.0 sCMOS camera (Hamamatsu Photonis Europe GmbH, Herrsching, Germany). Image sequences of individual particles (500 frames) were acquired using a 100× oil-immersion objective (HCX PL PLAPO 100C/1.47 NA). Excitation was provided by a 488-nm laser diode (4.54 mW at 10%), with a frame rate of 10 Hz (100 ms/frame). The evanescent field penetration depth was 90 nm. Movies were analyzed using the TrackAnalyzer [39] plugin in Fiji (version 1.53). The initial phase of the TrackAnalyzer workflow involves particle detection and trajectory generation utilizing TrackMate [40, 41]. Particles were identified by subpixel localization using a Laplacian of Gaussian (LoG) detector with an estimated object diameter of 0.5 μm, a quality threshold of 15, and median filtering enabled. Frame-to-frame spot linking was performed using the TrackMate Linear Assignment Problem (LAP) algorithm with closing gaps (maximum linking distance = 0.5 μm; gap closing distance = 0.1 μm; maximum gap = 6 frames). Only trajectories lasting at least 20 frames were retained for further analysis. Once all trajectories were identified, the mean spot intensity (MSI), the number of mobile and immobile particles, and diffusion coefficients ($D_{1\text{-}4}$) were calculated with TrackAnalyzer [39].

To determine the minimum detectable diffusion coefficient in our experimental conditions, we used Ac-GFP seeded onto glass coverslips (30 min). As 95% of the fixed GFP showed a diffusion coefficient ≤ 0.002 $\mu m^2\ s^{-1}$, this value was set as the threshold to discriminate between immobile and mobile trajectories (Supplementary Fig. 3B). The “Subtract Bg 4” method was used for background subtraction prior to the MSI calculation.

To estimate receptor number in individual trajectories, we used single-step photobleaching analysis of ACKR3-AcGFP spots (Supplementary Fig. 3C) to determine the MSI value that corresponds to monomers (MSI = 70 a.u.) (Supplementary Fig. 3C, D), and this value was then used as a reference to estimate the number of receptors/particle.

Dual-color TIRF imaging and analysis

JKX4-AcGFP-KI cells were transiently transfected with ACKR3–SNAP-tag and labeled with SNAP-Cell TMR-Star. Cells expressing low levels of receptors per cell (Supplementary Fig. 4A) were selected for detection and tracking analyses. Experiments were performed using the same TIRF microscope and camera. Excitation was provided by a 488-nm laser diode (3.96 mW at 6%) for CXCR4 and by a 561-nm laser diode (2.64 mW at 10%) for ACKR3, with a frame rate of 10 Hz (100 ms/frame). The evanescent field penetration depth was 103 nm for ACKR3 and 90 nm for CXCR4. Cross-talk between channels at the laser powers used in the experiments was ruled out by confirming the absence of signal in the red channel upon exciting untransfected JKX4-AcGFP-KI cells with the 488-nm laser diode (3.96 mW at 8%). Movies were first analyzed separately, channel-by-channel, using the TrackAnalyzer [39] plugin (version 1.53), applying the same parameters as previously described (green channel) for single-molecule TIRF experiments, although in this case frame-to-frame spot linking was performed without closing gaps. For ACKR3 (red channel), particles were identified by subpixel localization using a LoG detector with an estimated object diameter of 0.5 μm, a quality threshold of 9, and median filtering enabled. Frame-to-frame spot linking was performed using the TrackMate LAP algorithm without closing gaps (maximum linking distance = 0.5 μm), and only trajectories lasting at least 20 frames were retained for further analysis.

Dual-molecule TIRF analysis was performed by combining the independently processed fluorescence channels. Unlike single-molecule approaches based on a single channel, this dual-color strategy relies on the simultaneous acquisition of two spectrally distinct channels, enabling coordinated tracking and quantitative analysis of particle pairs. Trajectories were first filtered in each channel based on background-corrected fluorescence intensity within a defined frame range to retain only trajectories with signals suitable for reliable dual-color analysis. Subsequently, trajectories from both channels were compared frame-by-frame and considered associated when they exhibited temporal overlap for at least 10 frames and remained within a predefined x–y distance threshold of 0.4 μm. Tracks fulfilling these criteria

were classified as overlapping dual-color trajectories, indicative of coordinated spatial and temporal behavior consistent with molecular association or co-trafficking events, whereas tracks lacking a corresponding signal in the opposite channel were classified as non-overlapping.

For both overlapping and non-overlapping populations, trajectory-based parameters were quantified as in single-color TIRF analysis. The number of receptors along individual trajectories was determined as previously described, using single-step photobleaching analysis (Supplementary Fig. 4B) to obtain the intensity of the monomeric protein for ACKR3-SNAP-tag labeled with SNAP-Cell TMR-Star (MSI = 33 a.u.) (Supplementary Fig. 4C) and for CXCR4-AcGFP (MSI = 70 a.u.) (Supplementary Fig. 4D).

The custom analysis pipeline used for dual-molecule trajectory pairing and quantification is available as an open-source Python script on GitHub (https://github.com/acayuelalopez/Dual_Molecule_Track_Analysis.git), ensuring full reproducibility of the analysis.

Statistical analysis

All statistical analyses were conducted using GraphPad PRISM version 10 (ns = not significant; $*P \leq 0.05$; $**P \leq 0.01$; $***P \leq 0.001$; $****P \leq 0.0001$). A two-tailed, unpaired, nonparametric Mann-Whitney test was used to analyze CTCF immunofluorescence values. Data for MSI and diffusion coefficients ($D_{1–4}$) of single particles are presented as the median of each individual experiment, together with the mean of the medians and the mean of the first (Q1) and third (Q3) quartiles. To evaluate the effect of CXCL12 within the same cell line, a paired parametric *t*-test was used to analyze the mean of the medians for these measurements, as well as the percentage of receptors in oligomers and the percentage of immobile particles in TIRF-M experiments. Conversely, a two-tailed unpaired parametric *t*-test was used for comparative analysis between different cell lines. For flow cytometry, geometric mean differences in cell surface receptor expression were analyzed using a two-tailed paired parametric t-test within cell lines, and an unpaired parametric t-test between different cell lines. A two-tailed unpaired parametric t-test was also used to analyze ACKR3 CTCF immunofluorescence values between JK and JKA3$^{-/-}$ cells. Finally, a two-way ANOVA was applied to analyze receptor internalization by BRET, β-arrestin recruitment, actin polymerization, cell polarization, G-protein activation and recruitment, and cAMP inhibition.

Results

CXCL12 binding modulates ACKR3 dynamics and enhances receptor clustering

CXCR4 forms oligomers at the cell surface, the organization of which is dynamically modulated by CXCL12 binding [35]. These nanoscale complexes dictate downstream signaling pathways essential for cell migration and the sensing of chemoattractant gradients [36, 42]. While some reports suggest that ACKR3 in T cells functions primarily as a scavenger receptor with a predominantly intracellular distribution [21, 43], its translocation to the cell surface is a critical regulatory step. By facilitating the sequestration and removal of extracellular ligands, surface localized ACKR3 directly contributes to the maintenance and shaping of chemoattractant gradients. Using receptor-specific antibodies, we first characterized the expression pattern of endogenous ACKR3 in Jurkat cells, comparing those endogenously expressing CXCR4 (JK) with a CXCR4-deficient cell line (JKX4$^{-/-}$) [36]. In both cell types, ACKR3 was detectable at the plasma membrane; however, its surface expression levels were significantly lower in the absence of CXCR4 (Fig. 1A, B, D). By contrast, transferrin receptor, TfR, was equally expressed by both JK and JKX4$^{-/-}$ cells (Fig. 1A, C), serving as a control. These observations suggest that CXCR4 may facilitate the trafficking of intracellular ACKR3 to the cell surface. This aligns with the known ability of these receptors to form heterodimers [12, 13]. However, we observed no differences in CXCL12-mediated ACKR3 internalization between JK and JKX4$^{-/-}$ cells (Supplementary Fig. 5A, B). This suggests that ACKR3 internalization and recycling is not modulated by CXCR4 co-expression.

To evaluate ACKR3 dynamics at the cell membrane, we performed single-particle tracking (SPT) using TIRF-M. JK and JKX4$^{-/-}$ cells were transiently transfected with ACKR3 fused to monomeric GFP (ACKR3-AcGFP). To ensure high-fidelity SPT conditions and minimize tracking errors, only cells with a surface density <4.5 particles/μm^2 were included in the analysis. Individual receptor trajectories were generated using a validated tracking algorithm optimized for single-molecule analysis [40, 41].

In unstimulated cells, ACKR3 dynamic parameters were comparable across cell lines (Fig. 2A) (Supplementary video 1-4), with the majority of particles being classified as mobile (~87% in JK cells vs. ~83% in JKX4$^{-/-}$ cells) (Fig. 2B). CXCL12 stimulation (Fig. 2A) significantly reduced receptor diffusivity (median D_{1-4} = 0.009 μm^2 s^{-1}) in the membrane of both cell types (Fig. 2C), and increased the fraction of immobile particles from ~13% (unstimulated) to ~22% (CXCL12) and from ~17% (unstimulated) to ~23% (CXCL12) in JK and JKX4$^{-/-}$ cells, respectively (Fig. 2B). Under basal conditions, ACKR3 intensity distribution was similar across both cell lines (mean = 73 a.u. in JK vs. 70 a.u. in JKX4$^{-/-}$) and increased

significantly following CXCL12 stimulation (mean = 80 a.u. in JK vs. 77 a.u. in JKX4$^{-/-}$) (Fig. 2D). These baseline values indicate that ACKR3 exists predominantly as monomers and dimers in unstimulated cells (~99% in both JK and JKX4$^{-/-}$). However, CXCL12 treatment promoted higher-order organization, increasing the fraction of receptors within nanoclusters (~17% in nanoclusters containing ≥3 receptors in JK cells vs. ~9.5% in JKX4$^{-/-}$ cells) (Fig. 2E).

Distinguishing between agonist-mediated receptor nanoclustering, which facilitates cellular activation at the plasma membrane, and the receptor aggregation that precedes ligand-induced internalization can be challenging. This distinction was previously established for CXCR4 using internalization-deficient mutants that retained the ability to oligomerize in response to CXCL12 [35]. For ACKR3, discriminating between *bona fide* surface oligomers and internalization-associated aggregates is even more critical, given that the receptor constitutively internalizes and recycles to regulate ligand bioavailability [23]. Canonical chemokine receptor internalization typically requires agonist-induced receptor aggregation into clathrin-coated pits, a process that depends on GRK-mediated Ser/Thr phosphorylation of residues in the C-terminal tail and subsequent β-arrestin recruitment [44]. By contrast, while ACKR3 internalization depends on ligand-induced GRK phosphorylation, it has been shown to occur independently of β-arrestin engagement [27, 45, 46].

To confirm that the structures detected by TIRF-M represented functional ACKR3 oligomers rather than aggregates associated with receptor internalization, we used a C-terminal deletion mutant, ACKR3ΔCt, which lacks the GRK2 and GRK5 phosphorylation sites [46, 47]. We first verified that ACKR3ΔCt does not internalize using HEK-293 cells transiently transfected with CXCR4-, ACKR3-, or ACKR3ΔCt-RLuc8, together with rGFP-CAAX, a K-Ras-derived motif that anchors proteins to the inner leaflet of the plasma membrane [48]. Ligand-induced receptor internalization was monitored *via* BRET, where a decrease in the BRET signal reflects receptor endocytosis. As expected, CXCL12 triggered time-dependent internalization of both CXCR4 and ACKR3, while the selective agonist VUF15485 [37] induced internalization of ACKR3. By contrast, no agonist-induced internalization was observed for ACKR3ΔCt (Fig. 3A). These results confirm that ACKR3ΔCt is resistant to ligand-induced endocytosis, establishing it as a robust tool to distinguish between genuine surface oligomerization and the aggregates that precede internalization.

We next used CRISPR-Cas9 editing to generate an ACKR3-deficient Jurkat cell line (JKA3$^{-/-}$) by deleting the region AC079611.6:g[113769_113788del] (GenBank) across both alleles, eliminating the

initiator methionine in exon 4 (Supplementary Fig. 2). These cells were transiently transfected with ACKR3ΔCt-AcGFP and analyzed *via* SPT in TIRF-M mode to assess receptor oligomerization (Supplementary video 5, 6). Ligand stimulation significantly increased ACKR3ΔCt oligomerization (MSI value: 68 a.u. basal vs. 84 a.u. following CXCL12 treatment) (Fig. 3B). Under unstimulated conditions, ACKR3ΔCt-AcGFP was predominantly monomeric and dimeric, with only a small fraction (~2%) of receptors in oligomeric particles (≥3 receptors). Following CXCL12 stimulation, this fraction expanded to 19% (Fig. 3C), values consistent with those observed for ACKR3-AcGFP in parental JK cells (Fig. 2D, E). Overall, these results demonstrate that CXCL12 promotes ACKR3ΔCt oligomerization and confirm that receptor nanoclustering detected by TIRF-M represents genuine membrane organization rather than transient aggregates formed during the initiation of endocytosis.

Unlike CXCR4, ACKR3 is an atypical receptor that does not couple to Gi-proteins [49]. To confirm that CXCR4-mediated signaling was not required for CXCL12-induced ACKR3 clustering, we compared receptor dynamics in JK cells with and without pertussis toxin treatment (Supplementary video 7, 8). As expected, pertussis toxin had no effect on either the intensity distribution or the proportion of ACKR3 organized into large nanoclusters (Fig. 4A, B). By contrast, pertussis toxin treatment effectively blocked CXCL12-mediated CXCR4 nanoclustering (Fig. 4C, D) (Suplementary video 9-12), which served as a positive control for Gi-protein inhibition. Together with the data for JKX4$^{-/-}$ (Fig. 2), these results strongly suggest that CXCL12-mediated ACKR3 clustering occurs independently of CXCR4 expression and Gi-protein activation.

Ligand-binding is required for ACKR3 clustering

Experiments using JKX4$^{-/-}$ cells initially indicated that ACKR3 clustering is a CXCL12-dependent process. However, because CXCL12 is a shared agonist for both CXCR4 and ACKR3 [14], we sought to confirm these data using the selective ACKR3 agonist VUF15485 [37] and the inverse agonist VUF16840 [50] to modulate receptor activity independently of CXCR4. JK and JKX4$^{-/-}$ cells were transiently transfected with ACKR3-AcGFP, and SPT-TIRF-M experiments were performed to analyze ACKR3 dynamics (Supplementary video 13-18). Relative to unstimulated controls, both VUF15485 and CXCL12 significantly increased ACKR3 oligomerization. This effect was largely abolished by VUF16840 pretreatment (MSI values = 66 or 67 a.u. in controls vs. 83 or 89 a.u. in VUF15485-treated cells; 88 or 81 a.u. in CXCL12-treated cells and 65 a.u. or 66 a.u. in VUF16840+CXCL12 treated JK or JKX4$^{-/-}$ cells)

(Fig. 5A, C). Under basal conditions, only ~0.2% and ~1% of ACKR3 receptors were found in nanoclusters in JK and JKX4$^{-/-}$ cells, respectively. Stimulation with VUF15485 increased this population to ~21% in JK cells and to ~23% in JKX4$^{-/-}$ cells. As demonstrated in Figure 2, when cells were activated with CXCL12, the percentage of ACKR3 in oligomers (~21%), was higher in JK cells than in JKX4$^{-/-}$ cells (~12%) (Fig. 5B, D). It is possible that the presence of CXCL12-mediated CXCR4 oligomerization facilitates the presence of ACKR3 in these clusters and could explain the differences observed. Conversely, pretreatment with VUF16840 completely suppressed CXCL12-mediated cluster formation (~0.3%) (Fig. 5B, D). As a control, VUF16840 treatment did not promote any ACKR3 clustering in these cells (Fig. 5).

Altogether, these data indicate that ACKR3 oligomerization is an agonist-dependent process that occurs independently of CXCR4 expression and G-protein signaling. However, when both receptors are co-expressed, there is a notable synergistic effect of CXCL12, resulting in a higher proportion of ACKR3 incorporated into larger clusters.

β-arrestin engagement does not affect ligand-mediated ACKR3 oligomerization

Recent evidence indicates that CXCL12-mediated CXCR4 nanoclustering requires β-arrestin1, which scaffolds CXCR4 to the actin cytoskeleton *via* cofilin [36]. We therefore investigated whether ACKR3 similarly recruits β-arrestins using a NanoBiT bioluminescence complementation assay. HEK-293 cells were transiently co-transfected with ACKR3-smBiT and either human β-arrestin1-lgBiT or β-arrestin2-lgBiT. Bioluminescence measurements confirmed [9] that both CXCL12 (Fig. 6A) and the ACKR3 specific agonist VUF15485 (Fig. 6B) promoted the recruitment of both β-arrestins to ACKR3 with comparable intrinsic activity, although CXCL12 displayed ~7-fold higher potency (CXCL12: EC_{50} for β-arrestin1 = 2.3 × 10^{-8} M and EC_{50} for β-arrestin2 = 1.8 × 10^{-8} M; VUF15485: EC_{50} for β-arrestin1 = 1.47 × 10^{-7} M and EC_{50} for β-arrestin2 = 1.3 × 10^{-7} M). As a control, the C-terminal deletion mutant ACKR3ΔCt failed to recruit either β-arrestin1 or β-arrestin2 (Fig. 6C), as previously reported [51].

To investigate the requirement for β-arrestins in ligand-mediated ACKR3 nanoclustering, we employed CRISPR-Cas9 to generate JKX4$^{-/-}$ cells lacking β-arrestin1 and β-arrestin2 (triple knock out JKX4$^{-/-}$β1$^{-/-}$β2$^{-/-}$). This was achieved by deleting the region DQ314866.1:g.[9565_9602del]; [9565_9603del] (GenBank), which eliminates the splice acceptor of exon 11 in the β-arrestin2 gene (Supplementary Fig. 1). We then transiently transfected ACKR3-AcGFP into both cells types, JKX4$^{-/-}$β1$^{-/-}$

β2$^{-/-}$ and JKX4$^{-/-}$ (control) cells (Fig. 7A) (Supplementary video 19, 20). TIRF-M analysis revealed a comparable increase in ACKR3 oligomerization following CXCL12 activation (MSI values: JKX4$^{-/-}$ basal 63 a.u. vs. CXCL12 71 a.u.; JKX4$^{-/-}$β1$^{-/-}$β2$^{-/-}$ basal 66 a.u. vs. CXCL12 75 a.u.) (Fig. 7B). Furthermore, we quantified the proportion of receptors within large nanoclusters (≥3 receptors). Under basal conditions, nanocluster formation was minimal in both JKX4$^{-/-}$ (∼0.1%) and JKX4$^{-/-}$β1$^{-/-}$β2$^{-/-}$ (∼0.6%) cells. Following CXCL12 stimulation, the percentage of receptors included in these clusters increased to ∼7% in both JKX4$^{-/-}$ and JKX4$^{-/-}$β1$^{-/-}$β2$^{-/-}$ cells (Fig. 7C). These findings were further corroborated by TIRF-M analysis of JKA3$^{-/-}$ cells transiently transfected with ACKR3ΔCt. This mutant also exhibited robust ligand-induced oligomerization (~2% in unstimulated cells vs. ~19% after activation) (Fig. 3B, C). Collectively, these results demonstrate that, in contrast to the mechanism driving CXCL12-mediated CXCR4 oligomerization, ligand-induced ACKR3 nanoclustering occurs independently of β-arrestins.

We next examined whether ACKR3 activation modulates actin polymerization. Using flow cytometry and phalloidin staining in JK cells, we observed that CXCL12 induced actin polymerization *via* CXCR4; however, the ACKR3 ligand VUF15485 failed to elicit a similar response (Fig. 8A). These results indicate that this atypical chemokine receptor does not independently regulate actin dynamics. Immunofluorescence and confocal analysis confirmed these observations. Jurkat cells expressing CXCR4 exhibited correct cell polarization following CXCL12 stimulation, whereas those that only express ACKR3 (JKX4$^{-/-}$) did not (Fig. 8B, C). Overall, these data demonstrate that while ligand activation of ACKR3 promotes dose-dependent β-arrestin recruitment, this pathway contributes neither to receptor nanoclustering nor to ligand-mediated actin cytoskeleton rearrangements.

CXCR4 and ACKR3 form dynamic heterocomplexes at the cell membrane

Several reports indicate that ACKR3 heterodimerizes with CXCR4 at the cell surface [12, 28], providing a potential mechanism by which ACKR3 modulates CXCR4-mediated cell functions [13, 28]. To visualize the dynamics of these CXCR4/ACKR3 heterocomplexes at the plasma membrane, we transiently transfected knock-in JK cells expressing CXCR4-AcGFP (JKX4-AcGFP-KI) with ACKR3-SNAP-tag.

The spatial organization of both receptors was analyzed by SPT using dual-color TIRF-M. While CXCR4-AcGFP fluorescence was detected directly, ACKR3-SNAP-tag was visualized following labeling with the SNAP-Cell TMR-Star substrate. Analysis confirmed that both tagged receptors were expressed and localized at the cell membrane (Supplementary Fig. 4).

By simultaneously tracking individual fluorescently labeled receptors across two spectral channels (Fig. 9A) (Supplementary video 21-24), we observed that in the absence of stimulation, ~2% of all trajectories corresponded to CXCR4/ACKR3 heterocomplexes. This proportion increased to ~8% upon CXCL12 stimulation (Fig. 9B). To ensure the precision of our heterocomplex analysis, we restricted the dataset to particles exhibiting more than 10 consecutive co-localized frames (1 sec). Under basal conditions, ~98% of CXCR4 and ~89% of ACKR3 molecules within these complexes existed as monomers or heterodimers. Upon CXCL12 stimulation, ~23% of CXCR4 molecules within heterocomplexes transitioned into trimers or larger clusters, while this fraction reached ~32% for ACKR3 (Fig. 9C). Notably, heterocomplex formation required the simultaneous activation of both receptors. Complexes were not stabilized by stimulation with VUF15485 alone, which selectively activates ACKR3, or by CXCL12 stimulation in cells pretreated with the ACKR3 antagonist VUF16840 (Fig. 9B). Collectively, these results indicate that CXCR4/ACKR3 complex stabilization depends on the concurrent activation of both receptors. At the plasma membrane, these heterocomplexes coexist with their respective homo-oligomeric conformations in a highly dynamic equilibrium influenced by ligand availability.

ACKR3 expression regulates CXCL12-mediated G-protein activation via CXCR4

Several studies have suggested that ACKR3 expression modulates CXCR4-mediated G-protein activation. To investigate the functional relevance of CXCR4/ACKR3 heterocomplexes, we performed BRET experiments to assess the ability of CXCL12 to trigger G-protein activation through either CXCR4 or ACKR3. HEK-293 cells were transiently co-transfected with either pcDNA.3-CXCR4 or pcDNA.3-ACKR3, together with a pIRES vector containing specific Gα subunits ($G\alpha_i$, $G\alpha_o$ $G\alpha_q$ or $G\alpha_{13}$) fused to N-Luc [52]. The vector also included a Gβ−T2A-cpv-Gγ insert, which ensures equimolar expression of all G-protein subunits, whereas Gγ is tagged with circularly permutated mVenus. In this system, mVenus fluorescence after the addition of coelenterazine H is detected only when the G-protein subunits are assembled in their inactive state (Gαβγ). The addition of CXCL12 induced rapid and sustained activation of $G\alpha_i$, evidenced by a decrease in BRET resulting from Gβγ dissociation upon CXCR4 activation. This effect was not observed for $G\alpha_o$ $G\alpha_q$ or $G\alpha_{13}$ (Fig. 10A), confirming the specificity of CXCR4 for Gi-proteins. As previously reported[53], $G\alpha_i$ was not activated by CXCL12 binding to ACKR3 (Fig. 10B).

These data were further corroborated in HEK-293 cells transiently co-transfected with CXCR4-smBiT or ACKR3-smBiT together with lgBiT-mini$G\alpha_i$. Addition of coelenterazine H triggered

bioluminescence only in cells with CXCR4 in its active conformation, indicating that the atypical receptor, ACKR3, was unable to associate with mini$G\alpha_i$ (Fig. 10C).

We next examined whether ACKR3 co-expression modulates CXCR4-mediated Gi protein activation and coupling in response to CXCL12. BRET experiments also demonstrated that the presence of ACKR3 reduced the ability of CXCR4 to activate and recruit $G\alpha_i$ (Fig. 10D, E). As a control, we confirmed in all these experiments that CXCR4 expression was not affected by ACKR3 expression (Supplementary Fig. 6A, B).

Collectively, these results indicate that the interaction between ACKR3 and CXCR4 triggers conformational rearrangements within CXCR4/$G\alpha_i$ complexes, likely accounting for the previously observed alterations in CXCR4 signaling in the presence of ACKR3 [12, 13].

Next, using JK and JKA3$^{-/-}$ cells, which express equivalent levels of endogenous CXCR4 (Supplementary Fig. 6C, D), we confirmed the functional impact of ACKR3 expression on the CXCR4-mediated $G\alpha_i$ inhibition of cAMP production by adenylate cyclase [54]. As expected, CXCL12 stimulation reduced forskolin-induced cAMP accumulation in cells lacking ACKR3. However, the co-expression of ACKR3 downmodulated this inhibitory effect (Fig. 10F). Altogether, these findings indicate that ACKR3 modulates the conformation and dynamics of CXCR4 through hetero-oligomerization, thereby serving as a critical regulator of its downstream signaling pathways.

Discussion

Chemokines are critical regulators of cell migration and play essential roles in orchestrating immune and inflammatory responses. The chemokine CXCL12 signals through two distinct members of the GPCR family: the canonical receptor CXCR4 and the atypical receptor ACKR3. Ligand binding to CXCR4 activates heterotrimeric G_i-proteins to regulate directed cell movement. By contrast, ACKR3 does not activate G-proteins [17, 55, 56]; however, both receptors undergo phosphorylation by GRKs and recruit β-arrestins in response to CXCL12 [13, 51, 53]. ACKR3 is primarily recognized for its role in chemokine scavenging. It internalizes CXCL12, sorting the ligand to lysosomes for degradation before recycling back to the plasma membrane [55, 57]. Through this mechanism, ACKR3 regulates the bioavailability of CXCL12 in the extracellular environment, a key step for maintaining CXCR4 responsiveness under both physiological and pathological conditions [45, 58]. Furthermore, ACKR3 forms heterodimers with CXCR4 at the cell surface [12, 13, 28], directly modulating CXCR4-mediated $G\alpha_i$-activation and signaling [12, 13].

Our data indicate that ACKR3 surface expression increases in T cells upon CXCR4 co-expression, suggesting a functional relationship between the two receptors at the plasma membrane. This observation aligns with previous studies demonstrating an interdependence between CXCR4 and ACKR3 expression levels. For instance, in human induced pluripotent stem cells, CXCR4 silencing reduces ACKR3 membrane expression [59], while in interneurons, ACKR3 deletion modulates CXCR4 expression to fine-tune chemokine responsiveness [60, 61]. Although chemokine receptor internalization often leads to receptor degradation, several reports indicate that ACKR3 is not necessarily degraded following internalization. Instead, it undergoes continuous recycling between the plasma membrane and intracellular compartments [55], a process that regulates both CXCR4 expression and signaling. Notably, in our experiments, CXCR4 co-expression did not alter the extent of CXCL12-induced ACKR3 internalization or recycling. This contrasts with previous findings showing that RAMP3 attenuates ACKR3 internalization and scavenging without affecting CXCR4 endocytosis [62], further highlighting the distinct mechanistic pathways that govern the endocytic trafficking of these two receptors.

We also found that CXCL12-mediated $G\alpha_i$ association with CXCR4 was reduced upon ACKR3 co-expression. Given that ACKR3 does not couple to $G\alpha_I$ [27], and that we observed no decrease in CXCR4 expression in co-transfected cells, these findings suggest that ACKR3, *via* its interaction with CXCR4, modulates the structural orientation or accessibility of the CXCR4 binding pocket to $G\alpha_i$. The ability of ACKR3 to form heterodimers with CXCR4, impairing its capacity to activate Gi-proteins, alongside its established role in CXCL12 sequestration [26], underscores the profound modulatory influence of ACKR3 on CXCR4 function [13].

Studies using SPT-TIRF and super-resolution microscopy have demonstrated that CXCR4 exists at the plasma membrane in a dynamic equilibrium of monomers, dimers, and oligomers (groups of ≥3 receptors). CXCL12 binding shifts this distribution by depleting the monomer/dimer population in favor of large nanoclusters, thereby altering the lateral mobility and spatial organization of CXCR4 [35]. This nanoscale organization is essential for productive CXCR4 signaling and efficient directional cell migration in CXCL12 gradients [36].

We therefore examined the oligomerization dynamics of ACKR3. Our results demonstrate that ACKR3, similar to CXCR4, exists as a population of monomers, dimers, and nanoclusters. Binding of either CXCL12 or VUF15485 enhances the formation of these nanoclusters, which were found to be largely immobile. This oligomerization was independent of CXCR4 expression and, unlike CXCR4, was not

inhibited by pertussis toxin, consistent with the inability of ACKR3 to couple to Gi-proteins. Pretreatment with the selective ACKR3 antagonist VUF16840 abolished CXCL12-induced nanoclustering, indicating that while ACKR3 oligomerization requires agonist binding and receptor activation, it is independent of G-protein signaling.

When characterizing receptor oligomers at the plasma membrane, it is essential to distinguish functional oligomers from the protein aggregates involved in receptor endocytosis. Ligand-induced chemokine receptor internalization typically requires GRK-mediated phosphorylation of the C-terminal Ser/Thr residues, β-arrestin recruitment, and subsequent aggregation in clathrin-coated pits [63]. For CXCR4, we previously distinguished between these entities using the $CXCR4^{K239AV242AL246A}$ mutant, which fails to oligomerize in response to CXCL12 despite undergoing internalization [35], and AGR1.137, a negative allosteric modulator that blocks receptor oligomerization without affecting CXCL12 binding or endocytosis [64]. Given that ACKR3 undergoes constitutive internalization and recycling [26], distinguishing between oligomerization and endocytic aggregates is even more critical. Unlike canonical chemokine receptors, ACKR3 internalization is β-arrestin-independent and instead requires GRK2 and/or GRK5-mediated phosphorylation of the C-terminal tail [45]. By using a C-terminal deletion mutant, (ACKR3ΔCt) that cannot be phosphorylated or internalized, we observed that CXCL12 still induced robust oligomerization. These findings demonstrate that ACKR3 oligomers and internalization-associated aggregates are distinct membrane entities, confirming that ACKR3 nanoclustering is a specific process linked to receptor signaling rather than endocytosis.

CXCL12-induced CXCR4 oligomerization requires β-arrestin1 activation, which scaffolds the receptor to the actin cytoskeleton and facilitates remodeling through cofilin [36]. Using NanoBiT assays, we observed CXCL12-dependent recruitment of both β-arrestin1 and β-arrestin2 to ACKR3, consistent with previous reports [9, 53, 65]. However, our data indicate that ACKR3 still undergoes oligomerization in cells lacking β-arrestins. While β-arrestins are known to regulate actin cytoskeleton remodeling downstream of multiple GPCRs [66], we did not observe agonist-induced actin polymerization or cell polarization downstream of ACKR3. These observations align with previous findings that ACKR3 does not induce cell migration and that β-arrestins are dispensable for ACKR3-dependent regulation of neuronal migration [45].

Multiple studies have established that CXCR4 and ACKR3 form heterodimers [13, 67, 68]. We therefore investigated whether these CXCR4/ACKR3 complexes are dynamic hetero-oligomers and

whether their dynamic behavior is modulated by agonist stimulation. Using dual-color TIRF-M for the simultaneous detection of both receptors, we quantified heterocomplex formation and observed that these structures coexist with both CXCR4 and ACKR3 homo-oligomers. The lipid environment likely contributes to the spatial segregation of these homo- and hetero-oligomers. Membrane charge strongly influences chemokine binding; for instance, anionic lipids enhance the binding affinity of CXCL12 for ACKR3 [69]. Furthermore, lipid composition modulates CXCR4 conformation and dynamics[70, 71]. Consistent with these principles, we found that CXCR4/ACKR3 heterocomplexes are dynamic structures regulated by ligand binding. CXCL12, which activates both receptors, increased the proportion of heterocomplexes and the number of receptors incorporated into large clusters. By contrast, VUF15485, a selective ACKR3 agonist, decreased hetero-oligomerization while increasing complexes of only ACKR3. Furthermore, when cells were pretreated with the ACKR3 antagonist VUF16840, CXCL12 failed to increase CXCR4/ACKR3 heterocomplexes but still promoted CXCR4 nanoclustering. These findings indicate that chemokine receptors adopt distinct dynamic conformations at the plasma membrane depending on co-expression patterns and ligand availability, thereby contributing to signaling plasticity within complex chemokine environments. Recent structural data highlight marked differences in the conformational landscapes of these receptors. ACKR3 exhibits four conformational states, inactive R, active R*, R' (inactive-like) and R*' in roughly equal proportions, whereas CXCR4 occupies three major membrane states [72]. How these conformational equilibria influence homo- and hetero-oligomer formation remains an important question for future investigation. Heterodimerization between ACKR3 and CXCR4 has been linked to the attenuation of CXCL12/CXCR4 signaling [67]. Consistent with this, we observed reduced $G\alpha_i$ association with CXCR4 and diminished $G\alpha_i$ activation in cells co-expressing both receptors. These findings align with earlier evidence that ACKR3 induces conformational rearrangements within preassembled CXCR4/G-protein complexes, thereby impairing $G\alpha_i$-protein activation [13]. We further confirmed this functional attenuation by demonstrating a reduction in CXCL12-mediated inhibition of forskolin-induced cAMP production in cells co-expressing ACKR3 and CXCR4. The clinical significance of this modulation is underscored by the role of CXCL12 in distinct biological settings; for instance, in the presence of low levels of ADP, CXCL12 acts as a potent agonist that promotes platelet aggregation and adhesion, contributing to tissue injury in ischemic myocardium and brain [73].

Through its interaction with CXCR4, ACKR3 regulates CXCL12-induced signaling and thereby modulates CXCR4 functions in both homeostasis and disease. CXCR4/ACKR3 heterocomplexes may

influence CXCL12-mediated regenerative mechanisms in coronary artery disease [74]. Furthermore, ACKR3 regulates chemokine responsiveness in migrating neurons by directly modulating CXCR4 function [61]. In melanoma, the co-expression of CXCR4 and ACKR3 on $CD8^+$ T cells governs their retention within peritumoral lymphatic vessels, suggesting that these receptors cooperatively regulate T-cell migration [75]. Additionally, ACKR3 expressed in liver sinusoidal endothelial cells differentially regulates CXCR4 activity, influencing the critical balance between fibrosis and regeneration [76]. More broadly, the intensity of CXCL12/CXCR4 signaling fine-tunes the equilibrium between inflammatory and tissue repair during acute wound healing [77].

Together, our findings demonstrate that ACKR3 is not merely a chemokine scavenger, but also an active regulator of receptor architecture and signaling at the plasma membrane. By forming dynamic nanoclusters and assembling hetero-oligomers with CXCR4 in a ligand-regulated manner, ACKR3 reshapes CXCR4 lateral mobility, G-protein accessibility, and downstream responsiveness. This molecular interplay offers a unifying mechanism to explain the diverse physiological roles attributed to CXCR4/ACKR3 cooperation. The ability of ACKR3 to modulate the signaling strength and spatial organization of CXCR4 provides a nanoscale framework for understanding how chemokine gradients are interpreted in complex environments. These insights highlight receptor oligomerization as a critical layer of chemokine receptor regulation and suggest that targeting ACKR3-dependent nanoscale organization may offer new opportunities to fine-tune CXCL12-mediated responses in homeostasis, inflammation, and disease.

Bibliography

1. Cecchinato V, Martini V, Pirani E, et al (2023) The chemokine landscape: one system multiple shades. Front Immunol 14:117661. https://doi.org/10.3389/FIMMU.2023.1176619
2. Ulvmar MH, Hub E, Rot A (2011) Atypical chemokine receptors. Exp Cell Res 317:556–568. https://doi.org/10.1016/J.YEXCR.2011.01.012
3. Comerford I, McColl SR (2024) Atypical chemokine receptors in the immune system. Nat Rev Immunol 24:753–769. https://doi.org/10.1038/S41577-024-01025-5
4. Cancellieri C, Vacchini A, Locati M, et al (2013) Atypical chemokine receptors: from silence to sound. Biochem Soc Trans 41:231–236. https://doi.org/10.1042/BST20120246
5. Oldham WM, Hamm HE (2008) Heterotrimeric G protein activation by G-protein-coupled receptors. Nat Rev Mol Cell Biol 9:60–71. https://doi.org/10.1038/NRM2299
6. Szpakowska M, Legler DF, Offermanns S, et al (2025) Inclusion of ACKR5 in the systematic nomenclature of atypical chemokine receptors. Nat Rev Immunol 25:225–226. https://doi.org/10.1038/S41577-025-01135-8
7. Chevigné A, Legler DF, Rot A, et al (2025) International Union of Basic and Clinical Pharmacology. CXVIII. Update on the nomenclature for atypical chemokine receptors, including ACKR5. Pharmacol Rev 77:. https://doi.org/10.1124/pharmrev.124.001361

8. Hoffmann F, Müller W, Schütz D, et al (2012) Rapid uptake and degradation of CXCL12 depend on CXCR7 carboxyl-terminal serine/threonine residues. Journal of Biological Chemistry 287:28362–28377. https://doi.org/10.1074/jbc.M111.335679
9. Gerken OJ, Catone N, Legler DF (2024) Identification of critical residues at the C-terminal tip of ACKR4 regulating chemokine internalization and βarrestin involvement. Cell Commun Signal 22:576. https://doi.org/10.1186/S12964-024-01961-8
10. Kleist AB, Jenjak S, Sente A, et al (2022) Conformational selection guides β-arrestin recruitment at a biased G protein-coupled receptor. Science 377:222–228. https://doi.org/10.1126/SCIENCE.ABJ4922
11. Traore BS, Casella S, Couvineau P, et al (2026) GRK-dependent ACKR3 endocytosis and chemokine scavenging is independent of receptor phosphorylation and β-arrestin. bioRxiv 2026.05.11.724365. https://doi.org/10.64898/2026.05.11.724365
12. Sierro F, Biben C, Martínez-Muñoz L, et al (2007) Disrupted cardiac development but normal hematopoiesis in mice deficient in the second CXCL12/SDF-1 receptor, CXCR7. Proc Natl Acad Sci U S A 104:14759–14764. https://doi.org/10.1073/PNAS.0702229104
13. Levoye A, Balabanian K, Baleux F, et al (2009) CXCR7 heterodimerizes with CXCR4 and regulates CXCL12-mediated G protein signaling. Blood 113:6085–6093. https://doi.org/10.1182/BLOOD-2008-12-196618
14. Burns JM, Summers BC, Wang Y, et al (2006) A novel chemokine receptor for SDF-1 and I-TAC involved in cell survival, cell adhesion, and tumor development. J Exp Med 203:2201–2213. https://doi.org/10.1084/JEM.20052144
15. Szpakowska M, Dupuis N, Baragli A, et al (2016) Human herpesvirus 8-encoded chemokine vCCL2/vMIP-II is an agonist of the atypical chemokine receptor ACKR3/CXCR7. Biochem Pharmacol 114:14–21. https://doi.org/10.1016/j.bcp.2016.05.012
16. Ikeda Y, Kumagai H, Skach A, et al (2013) XModulation of circadian glucocorticoid oscillation via adrenal Opioid-CXCR7 Signaling alters emotional behavior. Cell 155: 1323-1336. https://doi.org/10.1016/j.cell.2013.10.052
17. Meyrath M, Szpakowska M, Zeiner J, et al (2020) The atypical chemokine receptor ACKR3/CXCR7 is a broad-spectrum scavenger for opioid peptides. Nat Commun 11:3033. https://doi.org/10.1038/S41467-020-16664-0
18. Gerrits H, Van Ingen Schenau DS, Bakker NEC, et al (2008) Early postnatal lethality and cardiovascular defects in CXCR7-deficient mice. Genesis 46:235–245. https://doi.org/10.1002/DVG.20387
19. Nagasawa T, Hirota S, Tachibana K, et al (1996) Defects of B-cell lymphopoiesis and bone-marrow myelopoiesis in mice lacking the CXC chemokine PBSF/SDF-1. Nature 382:635–638. https://doi.org/10.1038/382635A0
20. Klein KR, Karpinich NO, Espenschied ST, et al (2014) Decoy Receptor CXCR7 Modulates Adrenomedullin-Mediated Cardiac and Lymphatic Vascular Development. Dev Cell 30:528–540. https://doi.org/10.1016/J.DEVCEL.2014.07.012
21. Sánchez-Martín L, Estecha A, Samaniego R, et al (2011) The chemokine CXCL12 regulates monocyte-macrophage differentiation and RUNX3 expression. Blood 117:88–97. https://doi.org/10.1182/BLOOD-2009-12-258186
22. Infantino S, Moepps B, Thelen M (2006) Expression and regulation of the orphan receptor RDC1 and its putative ligand in human dendritic and B cells. J Immunol 176:2197–2207. https://doi.org/10.4049/JIMMUNOL.176.4.2197
23. Luker KE, Steele JM, Mihalko LA, et al (2010) Constitutive and chemokine-dependent internalization and recycling of CXCR7 in breast cancer cells to degrade chemokine ligands. Oncogene 29:4599–4610. https://doi.org/10.1038/ONC.2010.212
24. Balabanian K, Lagane B, Infantino S, et al (2005) The chemokine SDF-1/CXCL12 binds to and signals through the orphan receptor RDC1 in T lymphocytes. Journal of Biological Chemistry 280:35760–35766. https://doi.org/10.1074/jbc.M508234200
25. Valentin G, Haas P, Gilmour D (2007) The Chemokine SDF1a Coordinates Tissue Migration through the Spatially Restricted Activation of Cxcr7 and Cxcr4b. Current Biology 17:1026–1031. https://doi.org/10.1016/j.cub.2007.05.020
26. Boldajipour B, Mahabaleshwar H, Kardash E, et al (2008) Control of Chemokine-Guided Cell Migration by Ligand Sequestration. Cell 132:463–473. https://doi.org/10.1016/j.cell.2007.12.034
27. Schafer CT, Chen Q, Tesmer JJG, Handel TM (2023) Atypical Chemokine Receptor 3 “Senses” CXC Chemokine Receptor 4 Activation Through GPCR Kinase Phosphorylations. Mol Pharmacol 104:174–186. https://doi.org/10.1124/molpharm.123.000710

28. Décaillot FM, Kazmi MA, Lin Y, et al (2011) CXCR7/CXCR4 heterodimer constitutively recruits β-arrestin to enhance cell migration. Journal of Biological Chemistry 286:32188–32197. https://doi.org/10.1074/jbc.M111.277038
29. Hartman NC, Groves JT (2011) Signaling clusters in the cell membrane. Curr Opin Cell Biol 23:370–376. https://doi.org/10.1016/j.ceb.2011.05.003
30. Verstreken P, Bellen HJ (2002) Meaningless minis? Mechanisms of neurotransmitter-receptor clustering. Trends Neurosci 25:383–385. https://doi.org/10.1016/S0166-2236(02)02197-5
31. Germain RN (1997) T-cell signaling: The importance of receptor clustering. Current Biology 7: R640-R644. https://doi.org/10.1016/s0960-9822(06)00323-x
32. Cairo CW (2007) Signaling by committee: receptor clusters determine pathways of cellular activation. ACS Chem Biol 2:652–655. https://doi.org/10.1021/CB700214X
33. Krummel MF, Sjaastad MD, Wulfing CW, Davis MM (2000) Differential clustering of CD4 and CD3ζ during T cell recognition. Science (1979) 289:1349–1352. https://doi.org/10.1126/SCIENCE.289.5483.1349;ISSUE:ISSUE:DOI
34. Kao H, Lin J, Littman DR, et al (2008) Regulated movement of CD4 in and out of the immunological synapse. J Immunol 181:8248–8257. https://doi.org/10.4049/JIMMUNOL.181.12.8248
35. Martínez-Muñoz L, Rodríguez-Frade JM, Barroso R, et al (2018) Separating Actin-Dependent Chemokine Receptor Nanoclustering from Dimerization Indicates a Role for Clustering in CXCR4 Signaling and Function. Mol Cell 70:106-119.e10. https://doi.org/10.1016/j.molcel.2018.02.034
36. García-Cuesta EM, Rodríguez-Frade JM, Gardeta SR, et al (2022) Altered CXCR4 dynamics at the cell membrane impairs directed cell migration in WHIM syndrome patients. Proc Natl Acad Sci U S A 119: e2119483119. https://doi.org/10.1073/PNAS.2119483119
37. Zarca AM, Adlere I, Viciano CP, et al (2024) Pharmacological Characterization and Radiolabeling of VUF15485, a High-Affinity Small-Molecule Agonist for the Atypical Chemokine Receptor ACKR3. Mol Pharmacol 105:301–312. https://doi.org/10.1124/molpharm.123.000835
38. Bosma R, Nesheva D, Rijnsburger M, et al (2025) Inhibition of constitutive activity of the atypical chemokine receptor 3 by the small-molecule inverse agonist VUF16840. Mol Pharmacol 107:. https://doi.org/10.1016/j.molpha.2025.100085
39. Cayuela López A, García-Cuesta EM, Gardeta SR, et al (2023) TrackAnalyzer: A Fiji/ImageJ toolbox for a holistic analysis of tracks. Biological imaging 3:e18. https://doi.org/10.1017/S2633903X23000181
40. Tinevez JY, Perry N, Schindelin J, et al (2017) TrackMate: An open and extensible platform for single-particle tracking. Methods 115:80–90. https://doi.org/10.1016/j.ymeth.2016.09.016
41. Ershov D, Phan MS, Pylvänäinen JW, et al (2022) TrackMate 7: integrating state-of-the-art segmentation algorithms into tracking pipelines. Nat Methods 19:829–832. https://doi.org/10.1038/S41592-022-01507-1
42. Hauser MA, Schaeuble K, Kindinger I, et al (2016) Inflammation-Induced CCR7 Oligomers Form Scaffolds to Integrate Distinct Signaling Pathways for Efficient Cell Migration. Immunity 44:59–72. https://doi.org/10.1016/j.immuni.2015.12.010
43. Pacheco MO, Rocha FA, Aloia TPA, Marti LC (2022) Evaluation of Atypical Chemokine Receptor Expression in T Cell Subsets. Cells 11:4099. https://doi.org/10.3390/CELLS11244099
44. Neel NF, Schutyser E, Sai J, et al (2005) Chemokine receptor internalization and intracellular trafficking. Cytokine Growth Factor Rev 16:637–658. https://doi.org/10.1016/j.cytogfr.2005.05.008
45. Saaber F, Schütz D, Miess E, et al (2019) ACKR3 Regulation of Neuronal Migration Requires ACKR3 Phosphorylation, but Not β-Arrestin. Cell Rep 26:1473-1488.e9. https://doi.org/10.1016/j.celrep.2019.01.049
46. Zarca A, Perez C, van den Bor J, et al (2021) Differential Involvement of ACKR3 C-Tail in β-Arrestin Recruitment, Trafficking and Internalization. Cells 10:1–16. https://doi.org/10.3390/CELLS10030618
47. Chen Q, Schafer CT, Mukherjee S, et al (2025) Effect of phosphorylation barcodes on arrestin binding to a chemokine receptor. Nature 643:280–287. https://doi.org/10.1038/S41586-025-09024-9
48. Choy E, Chiu VK, Silletti J, et al (1999) Endomembrane trafficking of ras: The CAAX motif targets proteins to the ER and Golgi. Cell 98:69–80. https://doi.org/10.1016/S0092-8674(00)80607-8

49. Graham GJ, Locati M, Mantovani A, et al (2012) The biochemistry and biology of the atypical chemokine receptors. Immunol Lett 145:30–38. https://doi.org/10.1016/j.imlet.2012.04.004
50. Otun O, Aljamous C, Nero E Del, et al (2024) Conformational dynamics underlying atypical chemokine receptor 3 activation. Proc Natl Acad Sci U S A 121: e2404000121. https://doi.org/10.1073/PNAS.2404000121
51. Canals M, Scholten DJ, de Munnik S, et al (2012) Ubiquitination of CXCR7 controls receptor trafficking. PLoS One 7: e34192. https://doi.org/10.1371/JOURNAL.PONE.0034192
52. Schihada H, Shekhani R, Schulte G (2021) Quantitative assessment of constitutive G protein-coupled receptor activity with BRET-based G protein biosensors. Sci Signal 14:. https://doi.org/10.1126/SCISIGNAL.ABF1653
53. Rajagopal S, Kim J, Ahn S, et al (2010) Beta-arrestin- but not G protein-mediated signaling by the "decoy" receptor CXCR7. Proc Natl Acad Sci U S A 107:628–632. https://doi.org/10.1073/PNAS.0912852107
54. Busillo JM, Benovic JL (2007) Regulation of CXCR4 signaling. Biochim Biophys Acta Biomembr 1768:952–963. https://doi.org/10.1016/j.bbamem.2006.11.002
55. Naumann U, Cameroni E, Pruenster M, et al (2010) CXCR7 functions as a scavenger for CXCL12 and CXCL11. PLoS One 5: e9175. https://doi.org/10.1371/JOURNAL.PONE.0009175
56. Ödemis V, Boosmann K, Heinen A, et al (2010) CXCR7 is an active component of SDF-1 signalling in astrocytes and Schwann cells. J Cell Sci 123:1081–1088. https://doi.org/10.1242/JCS.062810
57. Thelen M, Thelen S (2008) CXCR7, CXCR4 and CXCL12: An eccentric trio? J Neuroimmunol 198:9–13. https://doi.org/10.1016/j.jneuroim.2008.04.020
58. Luker KE, Lewin SA, Mihalko LA, et al (2012) Scavenging of CXCL12 by CXCR7 promotes tumor growth and metastasis of CXCR4-positive breast cancer cells. Oncogene 31:4750–4758. https://doi.org/10.1038/ONC.2011.633
59. Ceholski DK, Turnbull IC, Pothula V, et al (2017) CXCR4 and CXCR7 play distinct roles in cardiac lineage specification and pharmacologic β-adrenergic response. Stem Cell Res 23:77–86. https://doi.org/10.1016/j.scr.2017.06.015
60. Wang Y, Li G, Stanco A, et al (2011) CXCR4 and CXCR7 Have Distinct Functions in Regulating Interneuron Migration. Neuron 69:61–76. https://doi.org/10.1016/j.neuron.2010.12.005
61. Sánchez-Alcañiz JA, Haege S, Mueller W, et al (2011) Cxcr7 Controls Neuronal Migration by Regulating Chemokine Responsiveness. Neuron 69:77–90. https://doi.org/10.1016/j.neuron.2010.12.006
62. Pfersdorf F, Romanazzi L, Rosenkilde MM, Gustavsson M (2025) Regulation of the chemokine receptors CXCR4 and ACKR3 by receptor activity-modifying proteins. Journal of Biological Chemistry 301:108055. https://doi.org/10.1016/J.JBC.2024.108055
63. Solari R, Offord RE, Remy S, et al (1997) Receptor-mediated endocytosis of CC-chemokines. Journal of Biological Chemistry 272:9617–9620. https://doi.org/10.1074/jbc.272.15.9617
64. García-Cuesta EM, Martínez P, Selvaraju K, et al (2024) Allosteric modulation of the CXCR4:CXCL12 axis by targeting receptor nanoclustering via the TMV-TMVI domain. eLife 13: Tabledoi.org/10.7554/ELIFE.93968
65. Perez Almeria C V., Otun O, Schlimgen R, et al (2025) Constitutive activity of an atypical chemokine receptor revealed by inverse agonistic nanobodies. Nat Commun 16:10828. https://doi.org/10.1038/S41467-025-65858-X
66. Min J, DeFea K (2011) β-arrestin-dependent actin reorganization: Bringing the right players together at the leading edge. Mol Pharmacol 80:760–768. https://doi.org/10.1124/mol.111.072470
67. Dicenta-Baunach V, Laspa Z, Schaale D, et al (2025) ACKR3 agonism induces heterodimerization with chemokine receptor CXCR4 and attenuates platelet function. Eur J Clin Invest 55: e14327. https://doi.org/10.1111/ECI.14327
68. Fumagalli A, Zarca A, Neves M, et al (2019) CXCR4/AckR3 phosphorylation and recruitment of interacting proteins: Key mechanisms regulating their functional status. Mol Pharmacol 96:794–808. https://doi.org/10.1124/mol.118.115360
69. Eberle SA, Gustavsson M (2024) Bilayer lipids modulate ligand binding to atypical chemokine receptor 3. Structure 32:1174-1183.e5. https://doi.org/10.1016/j.str.2024.04.018
70. Gardeta SR, García-Cuesta EM, Palacios BS, et al (2025) Cholesterol oxidase treatment impairs CXCR4-mediated T cell migration. Cell Commun Signal 23:444. https://doi.org/10.1186/S12964-025-02392-9
71. Gardeta SR, García-Cuesta EM, D'Agostino G, et al (2022) Sphingomyelin Depletion Inhibits CXCR4 Dynamics and CXCL12-Mediated Directed Cell Migration in Human T Cells. Front Immunol 13: 925559. https://doi.org/10.3389/FIMMU.2022.925559

72. Schafer CT, Pauszek RF, Gustavsson M, et al (2025) Distinct activation mechanisms of CXCR4 and ACKR3 revealed by single-molecule analysis of their conformational landscapes. eLife 13: RP100098. https://doi.org/10.7554/ELIFE.100098
73. Gear ARL, Suttitanamongkol S, Viisoreanu D, et al (2001) Adenosine diphosphate strongly potentiates the ability of the chemokines MDC, TARC, and SDF-1 to stimulate platelet function. Blood 97:937–945. https://doi.org/10.1182/BLOOD.V97.4.937
74. Rath D, Chatterjee M, Borst O, et al (2014) Expression of stromal cell-derived factor-1 receptors CXCR4 and CXCR7 on circulating platelets of patients with acute coronary syndrome and association with left ventricular functional recovery. Eur Heart J 35:386–394. https://doi.org/10.1093/EURHEARTJ/EHT448
75. Steele MM, Jaiswal A, Delclaux I, et al (2023) T cell egress via lymphatic vessels is tuned by antigen encounter and limits tumor control. Nat Immunol 24: 664–675. https://doi.org/10.1038/S41590-023-01443-Y
76. Ding B Sen, Cao Z, Lis R, et al (2014) Divergent angiocrine signals from vascular niche balance liver regeneration and fibrosis. Nature 505:97–102. https://doi.org/10.1038/NATURE12681
77. Leung TH, Snyder ER, Liu Y, et al (2015) A cellular, molecular, and pharmacological basis for appendage regeneration in mice. Genes Dev 29:2097–2107. https://doi.org/10.1101/GAD.267724.115

Statements & Declarations

The authors declare no conflicts of interest. The ethics approval and consent to participate are not applicable in this study.

Author Contributions

N.S-A contributes with formal analysis, investigation, methodology and figures preparation; E.M.G-C contributes software development, formal analysis, supervision, investigation, methodology, and review; S.R.G. contributes investigation; R.V. provided input into the project; M.A. contributes investigation and methodology; O.J.G. contributes investigation and methodology; R.A.B. contributes investigation; R.L. contributes chemical compounds; H.F.V. contributes chemical compounds; and review; A.C. contributes software development; N.M. provided input into the project; B.S.P. contributes investigation; J.M.R-F contributes investigation, formal analysis, supervision, methodology, figures preparation; D.L. contributes methodology, supervision, funding acquisition, and review and M.M. contributes conceptualization, supervision, funding acquisition, writing – original draft, writing – review and editing.

Figure legends

Fig. 1. CXCR4 expression increases the surface expression of ACKR3. (A) Representative confocal microscopy images of JK (wild-type) and JKX4$^{-/-}$ (CXCR4$^{-/-}$) cells. Cells were immunostained for the transferrin receptor (TfR) using an Alexa Fluor 647-conjugated antibody (red) and for ACKR3 using an anti-ACKR3 antibody followed by ant-mouse IgG-Alexa Fluor 488 (green). Shown is the brightfield image and the merged fluorescence channels (from left to right: brightfield, 638 nm channel, 488 nm channel, and merged image over brightfield). Scale bar: 5 μm. **(B)** Fiji-based quantification of the corrected total cell fluorescence (arbitrary units, a.u.) corresponding to ACKR3 staining. The median value is indicated in red ($n = 5$; ****$P \leq 0.0001$). **(C)** Quantification of TfR staining, performed as described in panel B. The median value is indicated in red ($n = 5$; n.s., not significant). **(D)** Normalization of ACKR3 labeling to TfR labeling. The median ACKR3/TfR is indicated in red ($n = 5$; ****$P \leq 0.0001$). Each circle in panels B, C, and D represents a single cell from a total population of 380 cells analyzed per experimental condition.

Fig. 2. CXCR4 expression modulates ligand-mediated ACKR3 nanoclustering. (A) Representative single-particle tracking (SPT) of ACKR3-AcGFP in JK and JKX4$^{-/-}$ cells. Cells were analyzed on coverslips coated with fibronectin (FN) alone or FN+CXCL12. Particle counts and cell numbers are as follows: JK cells on FN (15,457 particles in 117 cells); JK cells on FN+CXCL12 (23,653 particles in 113 cells); JKX4$^{-/-}$ cells on FN (10,341 particles in 112 cells); and JKX4$^{-/-}$ cells on FN+CXCL12 (20,588 particles in 112 cells) ($n = 4$). (**B)** Percentage of mobile and immobile ACKR3-AcGFP particles at the cell membrane of the indicated cell lines ($n = 4$; *$P \leq 0.05$; **$P \leq 0.01$). (**C)** Diffusion coefficients ($D_{1–4}$) of mobile single trajectories in JK and JKX4$^{-/-}$cells expressing ACKR3-AcGFP under the conditions described in (A). The horizontal red lines represent the mean of median values from individual experiments; black dots indicate the median values of individual experiments (n = 4; *$P \leq 0.05$, **$P \leq 0.01$). (**C)** (**D)** Mean spot intensity (MSI) distribution (arbitrary units, a.u.) from individual ACKR3-AcGFP trajectories on unstimulated and CXCL12-stimulated JK and JKX4$^{-/-}$ cells. The mean of MSI median values from individual experiments is indicated by a horizontal red line; black dots indicate the median of MSI values of the individual experiments ($n = 4$; *$P \leq 0.05$). (**E)** Frequency of ACKR3-AcGFP receptors organized into oligomers (≥3 receptors per particle) in unstimulated and CXCL12-stimulated JK and JKX4$^{-/-}$ cells ($n = 4$; ns = not significant; ***$P \leq 0.001$; ****$P \leq 0.0001$).

Fig. 3. The ACKR3 C-terminal tail is required for CXCL12-mediated internalization but not for nanoclustering. (A) CXCL12- or VUF15485-induced receptor internalization, monitored by BRET in HEK-293 cells transiently co-transfected with rGFP-CAAX and CXCR4-, ACKR3-, or ACKR3ΔCt-RLuc8 quantified by using the area under the curve (AUC) (n = 3; ns = not significant; ****$P \leq 0.0001$). **(B, C)** Single-particle tracking (SPT) analysis of ACKR3ΔCt-AcGFP in JKA3$^{-/-}$ cells on coverslips coated with fibronectin (FN) alone or FN+CXCL12: (3,208 particles in 72 cells on FN; 6,610 particles in 77 cells on FN+CXCL12) (n = 3). **(B)** Mean spot intensity (MSI) distribution (in arbitrary units, a.u.) of individual ACKR3ΔCt-AcGFP trajectories in unstimulated and CXCL12-stimulated JKA3$^{-/-}$ cells. The mean of MSI median values from individual experiments is indicated by a horizontal red line; black dots indicate the median of MSI values of individual experiments (n = 3; *$P \leq 0.05$). **(C)** Frequency of ACKR3ΔCt-AcGFP receptors organized into oligomers (≥3 receptors per particle) in unstimulated and CXCL12-stimulated JKA3$^{-/-}$ cells (n = 3; *$P \leq 0.05$).

Fig. 4. ACKR3 clustering occurs independently of CXCR4 signaling. (A,B) Single-particle tracking (SPT) analysis of ACKR3-AcGFP in JK cells treated or not with pertussis toxin (PTx) (2 h, 37ºC, 0.2 μg/ml) on coverslips coated with fibronectin (FN) or FN+CXCL12 (4,692 particles in 77 cells on FN; 12,758 particles in 67 cells on FN+CXCL12; for PTx-treated cells, 4,267 particles in 75 cells on FN; 10,538 particles in 65 cells on FN+CXCL12) (n = 3). **(C,D)** SPT analysis of CXCR4-AcGFP in JKX4$^{-/-}$ cells treated or not with PTx (2 h, 37ºC, 0.2 μg/ml) on coverslips coated with FN or FN+CXCL12 (4,147 particles in 77 cells on FN; 10,663 particles in 85 cells on FN+CXCL12; for PTx treated cells, 4,789 particles in 77 cells on FN; 6,732 particles in 77 cells on FN+CXCL12) (n = 3). **(A)** Mean spot intensity (MSI) distribution (arbitrary units, a.u.) from individual ACKR3-AcGFP trajectories on unstimulated and CXCL12-stimulated JK transfected cells previously treated with PTx or vehicle. The mean of MSI median values from individual experiments is indicated by a horizontal red line; black dots indicate the median of MSI values of individual experiments (n = 3; ns = not significant; *$P \leq 0.05$). **(B)** Frequency of ACKR3-AcGFP receptors organized into oligomers (≥3 receptors per particle) in cells as described in (A) (n = 3; ns = not significant; *$P \leq 0.05$). **(C)** Mean spot intensity (MSI) distribution (arbitrary units, a.u.) from individual CXCR4-AcGFP trajectories on unstimulated and CXCL12-stimulated JKX4$^{-/-}$ transfected cells previously treated with PTx or vehicle. The mean of MSI median values from individual experiments is indicated by a horizontal red line; black dots indicate the median of MSI values of individual experiments (n = 3; ns = not significant;

*$P \leq 0.05$). **(D)** Frequency of CXCR4-AcGFP receptors organized into oligomers (≥3 receptors per particle) in cells as described in (C) ($n = 3$; ns = not significant; *$P \leq 0.05$).

Fig. 5. ACKR3 clustering requires agonist binding. Single-particle tracking (SPT) analysis of ACKR3-AcGFP in JK **(A,B)** and JKX4$^{-/-}$ **(C,D)** cells on coverslips coated with fibronectin (FN) or FN+CXCL12. In JK cells (5,781 particles in 81 cells on FN; 22,058 particles in 83 cells on FN+CXCL12; 20,186 particles in 85 cells on FN+VUF15485; 1,683 particles in 78 cells on FN+VUF16840; 2,703 particles in 81 cells on VUF16840+CXCL12) ($n = 3$). In JKX4$^{-/-}$ cells (3,985 particles in 75 cells on FN; 11,728 particles in 85 cells on FN+CXCL12; 13,444 particles in 82 cells on FN+VUF15485; 1,500 particles in 82 cells on FN+VUF16840; 1,551 particles in 79 cells on VUF16840+CXCL12) ($n = 3$). As indicated, when needed cells activated with VUF15485 or VUF16860 (both 1μM) were also included. **(A)** Mean spot intensity (MSI) distribution (arbitrary units, a.u.) from individual ACKR3-AcGFP trajectories on unstimulated and CXCL12-stimulated JK transfected cells previously treated with the indicated compounds or vehicle. The mean of MSI median values from individual experiments is indicated by a horizontal red line; black dots indicate the median of MSI values of individual experiments ($n = 3$; ns = not significant; *$P \leq 0.05$, **$P \leq 0.01$). **(B)** Frequency of ACKR3-AcGFP receptors organized into oligomers (≥3 receptors per particle) in JK cells as described in (A) ($n = 3$; ns = not significant; *$P \leq 0.05$, **$P \leq 0.01$). **(C)** MSI distribution (arbitrary units, a.u.) from individual ACKR3-AcGFP trajectories on unstimulated and CXCL12-stimulated JKX4$^{-/-}$ transfected cells previously treated with the indicated compounds or vehicle. The mean of MSI median values from individual experiments is indicated by a horizontal red line; black dots indicate the median of MSI values of individual experiments ($n = 3$; ns = not significant; *$P \leq 0.05$, **$P \leq 0.01$). **(D)** Frequency of ACKR3-AcGFP receptors organized into oligomers (≥3 receptors per particle) in JKX4$^{-/-}$ cells as described in (C) ($n = 3$; ns = not significant; *$P \leq 0.05$).

Fig. 6. Agonist binding promotes β-arrestin recruitment to ACKR3. NanoBiT assays were performed in HEK-293 cells transiently co-transfected with ACKR3-smBiT and either human β-arrestin1- or β-arrestin2-lgBiT were stimulated with increasing concentrations of CXCL12 **(A)** or VUF15485 **(B)**. As a control **(C)**, β-arrestin recruitment was measured in HEK-293 cells expressing ACKR3ΔCt-smBiT and either human β-arrestin1 or β-arrestin2-lgBiT upon stimulation with graded concentrations of CXCL12. Data represent the mean area under the curve (AUC) ± SD ($n = 4$).

Fig. 7. CXCL12-mediated ACKR3 oligomerization is independent of β-arrestin expression. (A) Analysis of CXCL12-mediated ACKR3 nanoclusters in JKX4$^{-/-}$ and JKX4$^{-/-}$β1$^{-/-}$β2$^{-/-}$ cells. Single-particle tracking (SPT) analysis of ACKR3-AcGFP in JKX4$^{-/-}$ and JKX4$^{-/-}$β1$^{-/-}$β2$^{-/-}$ cells on coverslips coated with fibronectin (FN) or FN+CXCL12 (4,529 particles in 69 JKX4$^{-/-}$ cells on FN; 12,221 particles in 68 JKX4$^{-/-}$ cells on FN+CXCL12; 5,350 particles in 69 JKX4$^{-/-}$β1$^{-/-}$β2$^{-/-}$ cells on FN; 13,236 particles in 67 JKX4$^{-/-}$ β1$^{-/-}$β2$^{-/-}$ cells on FN+CXCL12 in JKX4$^{-/-}$ cells) (n = 3). **(B)** Mean spot intensity (MSI) distribution (arbitrary units, a.u.) from individual ACKR3-AcGFP trajectories on unstimulated and CXCL12-stimulated JKX4$^{-/-}$ and JKX4$^{-/-}$β1$^{-/-}$β2$^{-/-}$ transfected cells. The mean of MSI median values from individual experiments is indicated by a horizontal red line; black dots indicate the median MSI values of individual experiments (n = 3; ns = not significant; *$P \leq 0.05$, **$P \leq 0.01$). **(C)** Frequency of ACKR3-AcGFP receptors organized into oligomers (≥3 receptors per particle) in unstimulated and CXCL12-stimulated JKX4$^{-/-}$ and JKX4$^{-/-}$β1$^{-/-}$β2$^{-/-}$ cells (n = 3; ns = not significant; *$P \leq 0.05$).

Fig. 8. Ligand binding on ACKR3 does not modulate actin cytoskeleton. (A) Actin polymerization in response to CXCL12 or VUF15485, as determined by F-actin (phalloidin-TRITC) staining in JK cells. Statistical significance was calculated for each time point relative to the unstimulated control (mean ± SD; n = 3; *$P \leq 0.05$, ***$P \leq 0.001$). **(B)** Representative images of a polarized and a non-polarized cell. Red: phalloidin-TRITC, green: anti-ICAM3-Alexa fluor 488. **(C)** Percentage of polarized JK and JKX4$^{-/-}$ cells adhered to fibronectin and treated or not with CXCL12, analyzed by immunostaining with anti-ICAM3-Alexa fluor 488 and phalloidin-TRITC. More than 1,500 cells were analyzed per condition. Data are presented as the percentage of polarized cells (mean ± SD; n = 3; ns = not significant; ****$P < 0.0001$).

Fig. 9. ACKR3 and CXCR4 form dynamic heterocomplexes at the plasma membrane. (A) Representative 3D (X-position/Y-position/time) profile of red and green particles from a dual-color TIRF experiment. The trajectories (red and green lines) illustrate the temporal (s) and spatial (μm) overlap of both fluorophores, indicating the formation of heterocomplexes in a subset of frames. **(B)** Percentage of CXCR4/ACKR3 heterocomplexes (≥3 receptors per particle) in unstimulated, CXCL12-, VUF15485- and VUF16860+CXCL12-stimulated knock-in JK cells expressing CXCR4-AcGFP (JKX4-AcGFP-KI) and transfected with ACKR3-SNAP-tag. Single-particle tracking (SPT) analysis was developed using 325 dual

trajectories in 134 unstimulated cells, 1,820 in 156 CXCL12 stimulated cells, 107 in 69 VUF15485-stimulated cells. No dual trajectories in 60 VUF16860+CXCL12-stimulated cells were detected. Data represent the mean ± SD ($n = 4$; ns = not significant; ***$P \leq 0.001$). **(C)** Oligomeric organization of CXCR4 and ACKR3 within CXCR4/ACKR3 heterocomplexes. The percentage of each receptor in monomer/dimer states or oligomers (≥3 receptors per particle) is shown for cells as described in (B). Data represent the mean ± SEM ($n = 4$; *$P \leq 0.05$).

Fig. 10. ACKR3 co-expression modulates CXCR4-mediated G-protein activation by CXCL12. **(A)** HEK-293 cells were transiently co-transfected with pcDNA.3-CXCR4, and a pIRES vector encoding NanoLuc (Nluc)-fused $G\alpha_i$, $G\alpha_o$, $G\alpha_q$, or $G\alpha_{13}$ as well as a Gβ–T2A–cpV–Gγ construct. Cells were stimulated with increasing concentrations of CXCL12. Data represent the mean area under the curve (AUC) ± SD ($n = 3$; ***$P \leq 0.001$; ****$P \leq 0.0001$). **(B)** G protein activation upon addition of increasing concentrations of CXCL12 in HEK-293 cells transiently co-transfected with pcDNA.3-ACKR3, and a pIRES vector encoding Nluc-fused $G\alpha_i$ or $G\alpha_q$ together with a Gβ–T2A–cpV–Gγ construct. ($n = 3$). **(C)** HEK-293 cells were transiently co-transfected with lgBiT-Mini$G\alpha_i$ and either CXCR4-smBiT or ACKR3-smBiT, and then stimulated with increasing concentrations of CXCL12. Data represent the mean AUC ± SD ($n = 3$; **$P \leq 0.01$; ****$P \leq 0.0001$). **(D)** HEK-293 cells were transiently co-transfected with pcDNA.3-CXCR4, an empty vector or ACKR3, as well as a pIRES vector encoding Nluc-fused $G\alpha_i$ and a Gβ–T2A–cpV–Gγ construct. Cells were stimulated with increasing concentrations of CXCL12 ($n = 3$; *$P \leq 0.05$; **$P \leq 0.01$; ***$P \leq 0.001$; ****$P \leq 0.0001$). **(E)** HEK-293 cells transiently co-transfected with lgBiT-Mini$G\alpha_i$ and CXCR4-smBiT, in the presence of an empty vector or ACKR3, were treated with increasing amounts of CXCL12. Values were normalized to the highest concentration added to CXCR4 expressing cells. ($n = 3$; **$P \leq 0.01$; ***$P \leq 0.001$). **(F)** JK and JKA3$^{-/-}$ cells were either unstimulated or stimulated with CXCL12 (50 nM, 5 min, 37°C), followed by forskolin treatment (10 μM, 10 min, 37°C) or left untreated (basal condition). Cells were lysed, and intracellular cAMP levels were quantified. Data are presented as the mean ± SD ($n = 4$; ns = not significant; *$P \leq 0.05$; ****$P \leq 0.0001$).

FIGURE 1

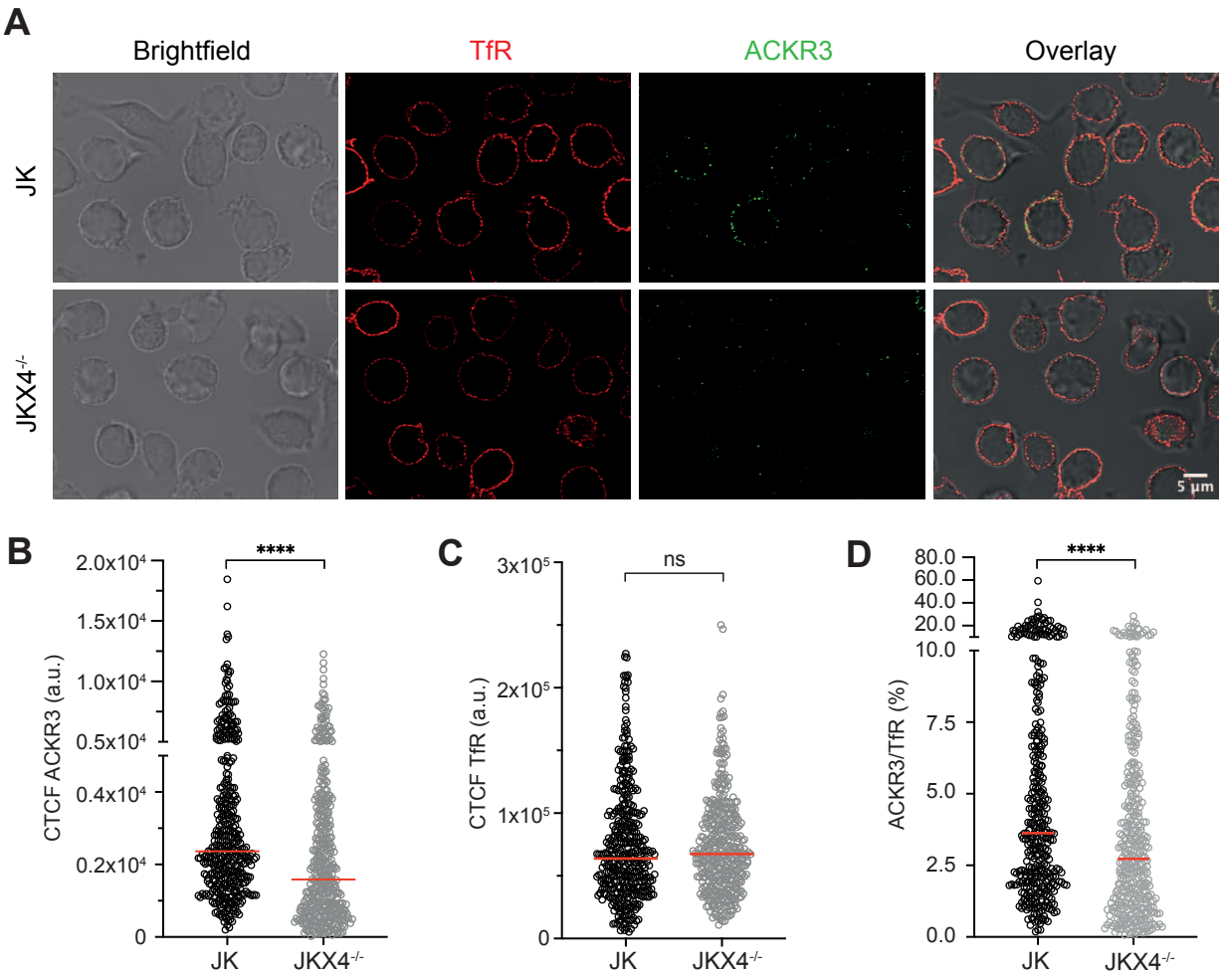


Figure 1. CXCR4 expression increases the surface expression of ACKR3. (A) Representative confocal microscopy images of JK (wild-type) and JKX4$^{-/-}$ (CXCR4$^{-/-}$) cells. Cells were immunostained for the transferrin receptor (TfR) using an Alexa Fluor 647-conjugated antibody (red) and for ACKR3 using an anti-ACKR3 antibody followed by anti-mouse IgG-Alexa Fluor 488 (green). Shown is the brightfield image and the merged fluorescence channels (from left to right: brightfield, 638 nm channel, 488 nm channel, and merged image over brightfield). Scale bar: 5 µm. **(B)** Fiji based quantification of the corrected total cell fluorescence (arbitrary units, a.u.) corresponding to ACKR3 staining. The median value is indicated in red (n = 5; ****P ≤ 0.0001). **(C)** Quantification of TfR staining, performed as described in panel B. The median value is indicated in red (n = 5; n.s., not significant). **(D)** Normalization of ACKR3 labeling to TfR labeling. The median ACKR3/TfR is indicated in red (n = 5; ****P ≤ 0.0001). Each circle in panels B, C, and D represents a single cell from a total population of 380 cells analyzed per experimental condition.

FIGURE 2

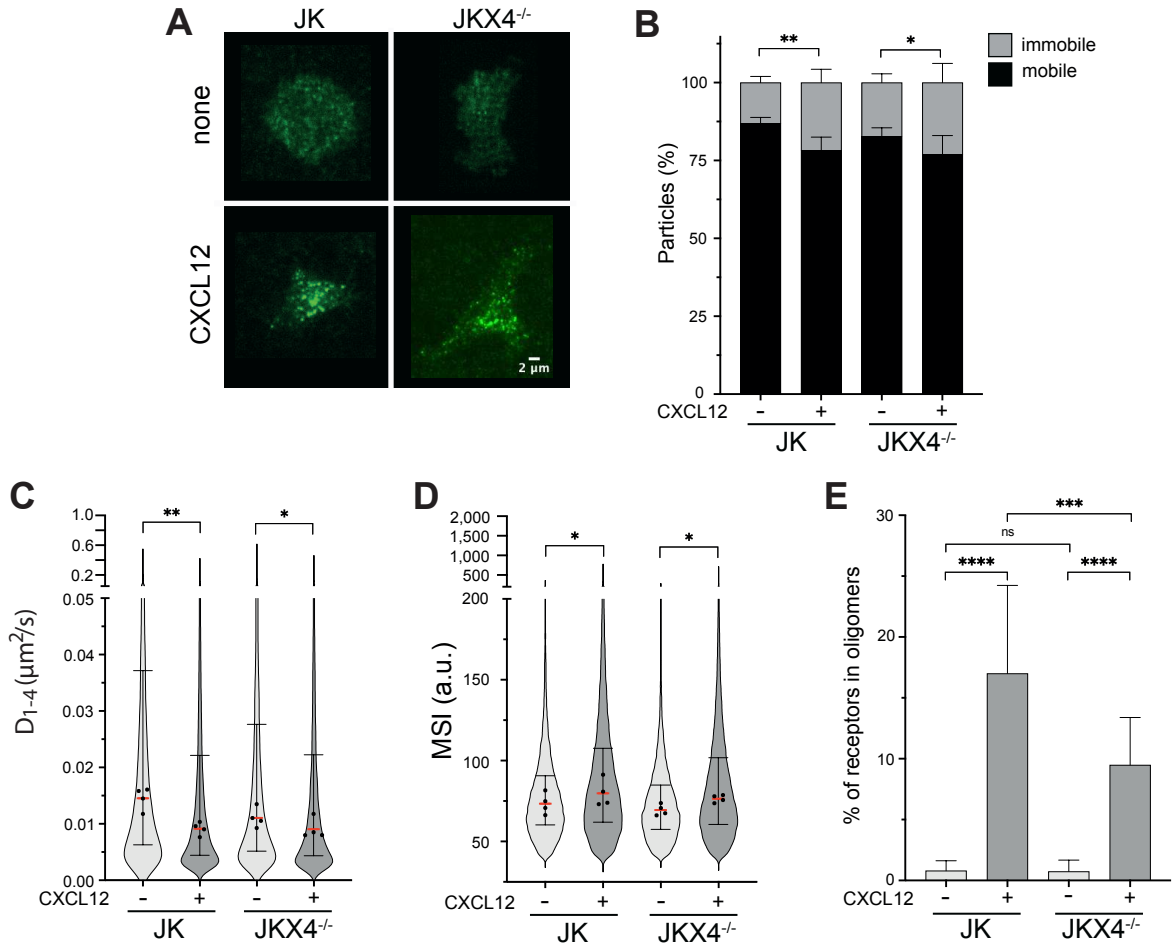


Figure 2. CXCR4 expression modulates ligand-mediated ACKR3 nanoclustering. (A) Representative single-particle tracking (SPT) of ACKR3-AcGFP in JK and JKX4$^{-/-}$ cells. Cells were analyzed on coverslips coated with fibronectin (FN) alone or FN+CXCL12. Particle counts and cell numbers are as follows: JK cells on FN (15,457 particles in 117 cells); JK cells on FN+CXCL12 (23,653 particles in 113 cells); JKX4$^{-/-}$ cells on FN (10,341 particles in 112 cells); and JKX4$^{-/-}$ cells on FN+CXCL12 (20,588 particles in 112 cells) (n = 4). **(B)** Percentage of mobile and immobile ACKR3-AcGFP particles at the cell membrane of the indicated cell lines (n = 4; *P ≤ 0.05; **P ≤ 0.01). **(C)** Diffusion coefficients ($D_{1–4}$) of mobile single trajectories in JK and JKX4$^{-/-}$ cells expressing ACKR3-AcGFP under the conditions described in (A). The horizontal red lines represent the mean of median values from individual experiments; black dots indicate the median values of individual experiments (n = 4; *P ≤ 0.05, **P ≤ 0.01). **(D)** Mean spot intensity (MSI) distribution (arbitrary units, a.u.) from individual ACKR3-AcGFP trajectories on unstimulated and CXCL12-stimulated JK and JKX4$^{-/-}$ cells. The mean of MSI median values from individual experiments is indicated by a horizontal red line; black dots indicate the median of MSI values of the individual experiments (n = 4; *P ≤ 0.05). **(E)** Frequency of ACKR3-AcGFP receptors organized into oligomers (≥3 receptors per particle) in unstimulated and CXCL12-stimulated JK and JKX4$^{-/-}$ cells (n = 4; ns = not significant; ***P ≤ 0.001; ****P ≤ 0.0001).

FIGURE 3

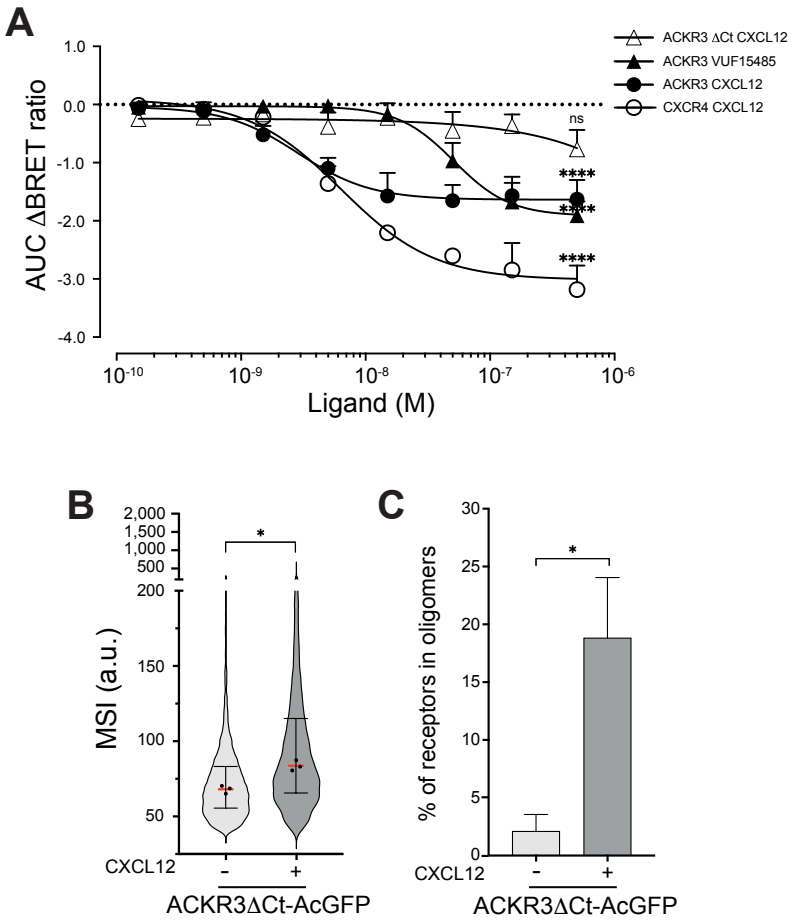


Figure 3. The ACKR3 C-terminal tail is required for CXCL12-mediated internalization but not for nanoclustering. (A) CXCL12 or VUF15485-induced receptor internalization, monitored by BRET in HEK-293 cells transiently co-transfected with rGFP-CAAX and CXCR4- , ACKR3- , or ACKR3Δ Ct-RLuc8 quantified by using the area under the curve (AUC) ± SD (n = 3; ns = not significant; ****P ≤ 0.0001). **(B, C)** Single-particle tracking (SPT) analysis of ACKR3ΔCt-AcGFP in JKA3$^{-/-}$ cells on coverslips coated with fibronectin (FN) alone or FN+CXCL12: (3,208 particles in 72 cells on FN; 6,610 particles in 77 cells on FN+CXCL12) (n = 3). **(B)** Mean spot intensity (MSI) distribution (in arbitrary units, a.u.) of individual ACKR3ΔCt-AcGFP trajectories in unstimulated and CXCL12-stimulated JKA3$^{-/-}$ cells. The mean of MSI median values from individual experiments is indicated by a horizontal red line; black dots indicate the median of MSI values of individual experiments (n = 3; *P ≤ 0.05). **(C)** Frequency of ACKR3ΔCt-AcGFP receptors organized into oligomers (≥3 receptors per particle) in unstimulated and CXCL12-stimulated JKA3$^{-/-}$ cells (n = 3; *P ≤ 0.05).

FIGURE 4

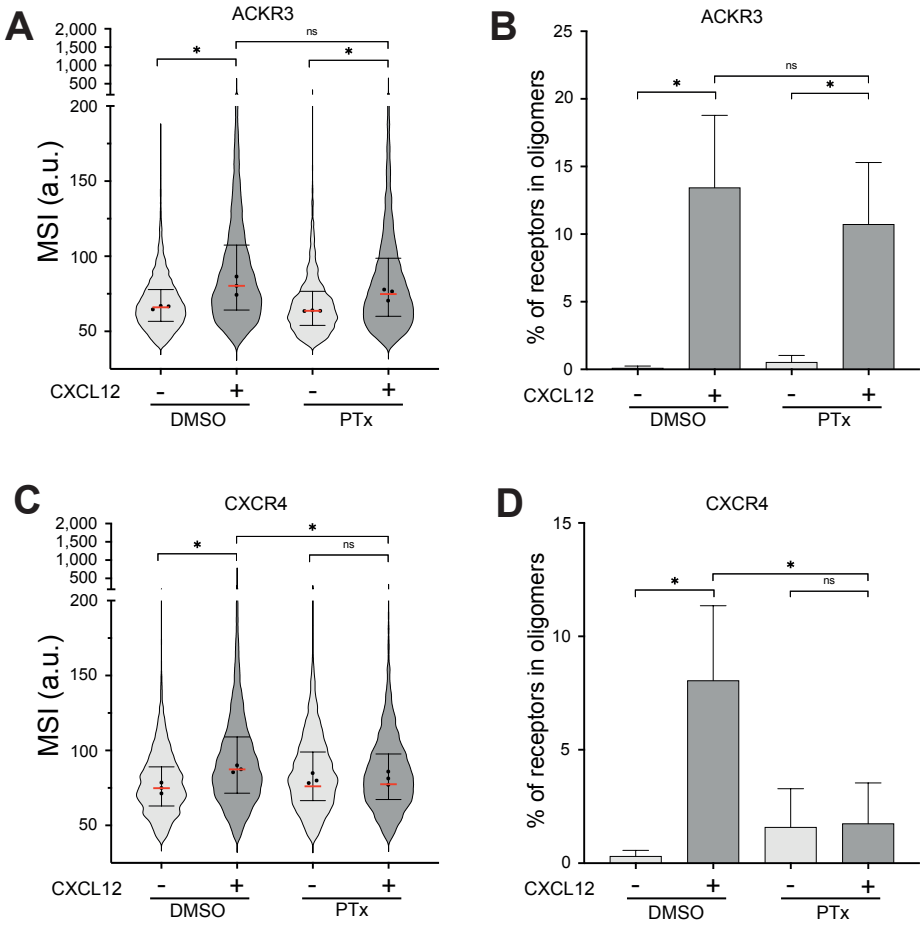


Figure 4. ACKR3 clustering occurs independently of CXCR4 signaling. (A,B) Single-particle tracking (SPT) analysis of ACKR3-AcGFP in JK cells treated or not with pertussis toxin (PTx) (2 h, 37ºC, 0.2 μg/ml) on coverslips coated with fibronectin (FN) or FN+CXCL12 (4,692 particles in 77 cells on FN; 12,758 particles in 67 cells on FN+CXCL12; for PTx-treated cells, 4,267 particles in 75 cells on FN; 10,538 particles in 65 cells on FN+CXCL12) (n = 3). **(C,D)** SPT analysis of CXCR4-AcGFP in JKX4$^{-/-}$ cells treated or not with PTx (2 h, 37ºC, 0.2 μg/ml) on coverslips coated with FN or FN+CXCL12 (4,147 particles in 77 cells on FN; 10,663 particles in 85 cells on FN+CXCL12; for PTx treated cells, 4,789 particles in 77 cells on FN; 6,732 particles in 77 cells on FN+CXCL12) (n = 3). **(A)** Mean spot intensity (MSI) distribution (arbitrary units, a.u.) from individual ACKR3-AcGFP trajectories on unstimulated and CXCL12-stimulated JK transfected cells previously treated with PTx or vehicle. The mean of MSI median values from individual experiments is indicated by a horizontal red line; black dots indicate the median of MSI values of individual experiments (n = 3; ns = not significant; *P ≤ 0.05). **(B)** Frequency of ACKR3-AcGFP receptors organized into oligomers (≥3 receptors per particle) in cells as described in (A) (n = 3; ns = not significant; *P ≤ 0.05). **(C)** Mean spot intensity (MSI) distribution (arbitrary units, a.u.) from individual CXCR4-AcGFP trajectories on unstimulated and CXCL12-stimulated JKX4$^{-/-}$ transfected cells previously treated with PTx or vehicle. The mean of MSI median values from individual experiments is indicated by a horizontal red line; black dots indicate the median of MSI values of individual experiments (n = 3; ns = not significant; *P ≤ 0.05). **(D)** Frequency of CXCR4-AcGFP receptors organized into oligomers (≥3 receptors per particle) in cells as described in (C) (n = 3; ns = not significant; *P ≤ 0.05).

FIGURE 5

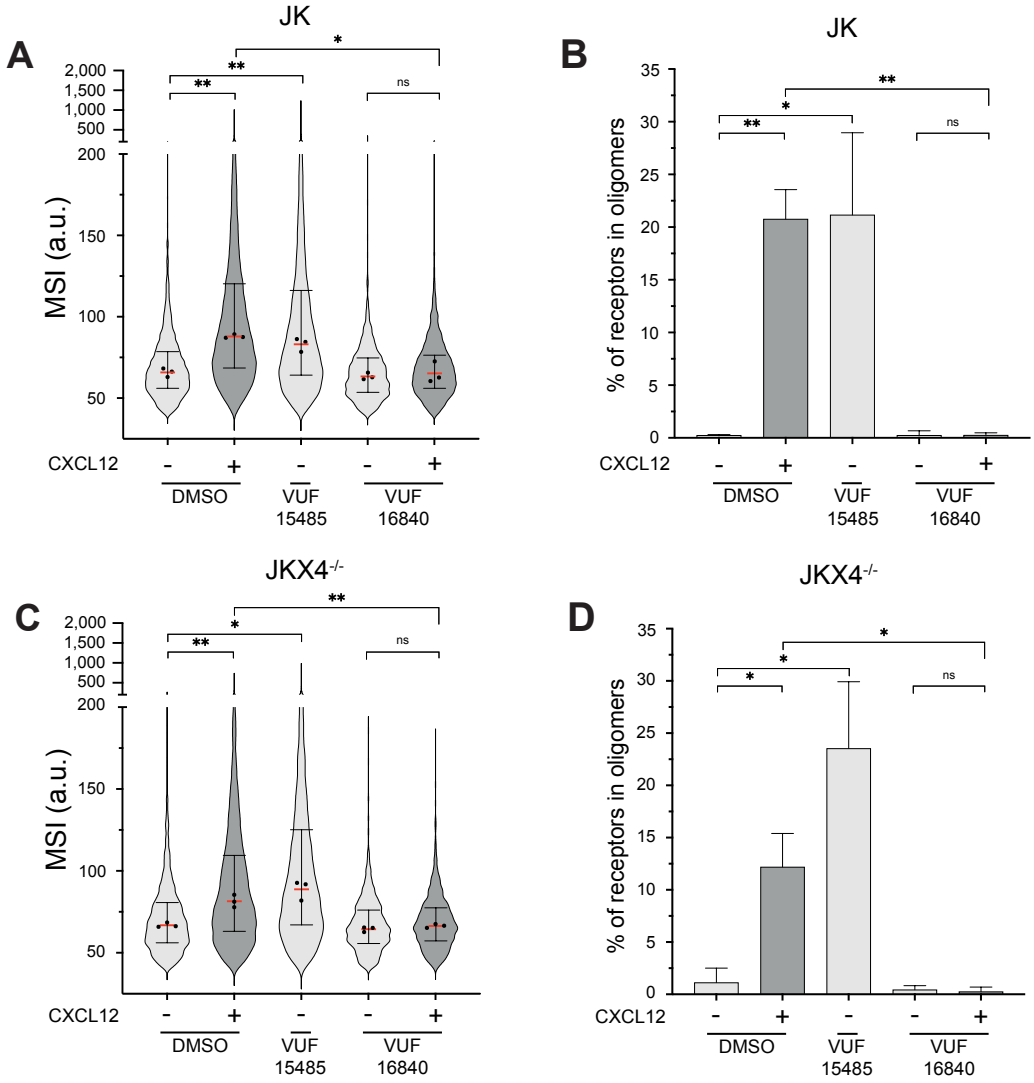


Figure 5. ACKR3 clustering requires agonist binding. Single-particle tracking (SPT) analysis of ACKR3-AcGFP in JK (A,B) and JKX4$^{-/-}$ (C,D) cells on coverslips coated with fibronectin (FN) or FN+CXCL12. In JK cells (5,781 particles in 81 cells on FN; 22,058 particles in 83 cells on FN+CXCL12; 20,186 particles in 85 cells on FN+VUF15485; 1,683 particles in 78 cells on FN+VUF16840; 2,703 particles in 81 cells on VUF16840+CXCL12) (n = 3). In JKX4$^{-/-}$ cells (3,985 particles in 75 cells on FN; 11,728 particles in 85 cells on FN+CXCL12; 13,444 particles in 82 cells on FN+VUF15485; 1,500 particles in 82 cells on FN+VUF16840; 1,551 particles in 79 cells on VUF16840+CXCL12) (n = 3). As indicated, when needed cells activated with VUF15485 or VUF16860 (both 1μM) were also included. **(A)** Mean spot intensity (MSI) distribution (arbitrary units, a.u.) from individual ACKR3-AcGFP trajectories on unstimulated and CXCL12-stimulated JK transfected cells previously treated with the indicated compounds or vehicle. The mean of MSI median values from individual experiments is indicated by a horizontal red line; black dots indicate the median of MSI values of individual experiments (n = 3; ns = not significant; *P ≤ 0.05, **P ≤ 0.01). **(B)** Frequency of ACKR3-AcGFP receptors organized into oligomers (≥3 receptors per particle) in JK cells as described in (A) (n = 3; ns = not significant; *P ≤ 0.05, **P ≤ 0.01). **(C)** MSI distribution (arbitrary units, a.u.) from individual ACKR3-AcGFP trajectories on unstimulated and CXCL12-stimulated JKX4$^{-/-}$ transfected cells previously treated with the indicated compounds or vehicle. The mean of MSI median values from individual experiments is indicated by a horizontal red line; black dots indicate the median of MSI values of individual experiments (n = 3; ns = not significant; *P ≤ 0.05, **P ≤ 0.01). **(D)** Frequency of ACKR3-AcGFP receptors organized into oligomers (≥3 receptors per particle) in JKX4$^{-/-}$ cells as described in (C) (n = 3; ns = not significant; *P ≤ 0.05).

FIGURE 6

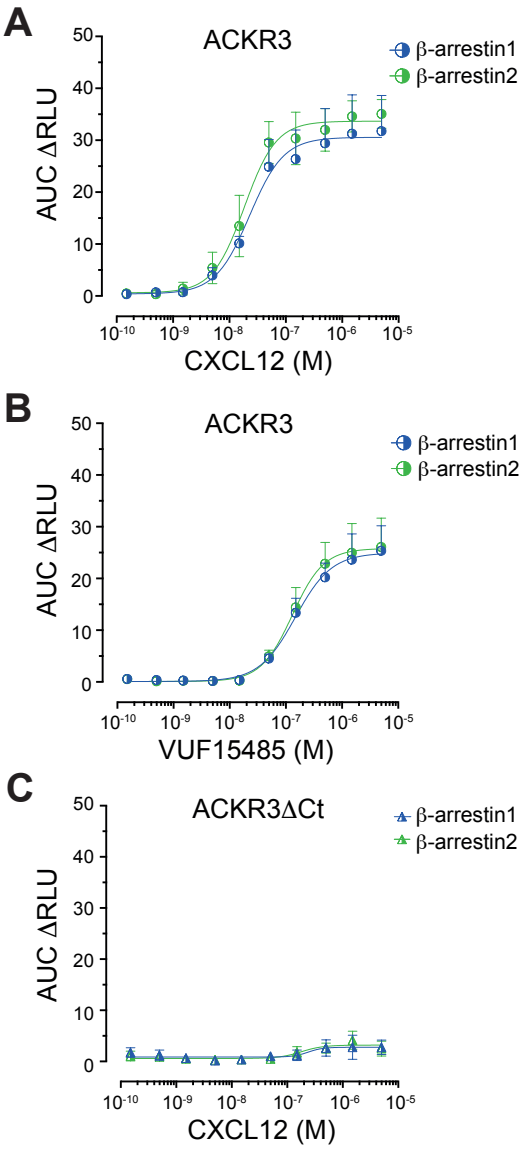


Figure 6. Agonist binding promotes β-arrestin recruitment to ACKR3. NanoBiT assays were performed in HEK-293 cells transiently co-transfected with ACKR3-smBiT and either human β-arrestin1- or β-arrestin2-lgBiT were stimulated with increasing concentrations of CXCL12 **(A)** or VUF15485 **(B)**. As a control **(C)**, β-arrestin recruitment was measured in HEK-293 cells expressing ACKR3ΔCt-smBiT and either human β-arrestin1 or β-arrestin2-lgBiT upon stimulation with graded concentrations of CXCL12. Data represent the mean area under the curve (AUC) ± SD (n = 4).

FIGURE 7

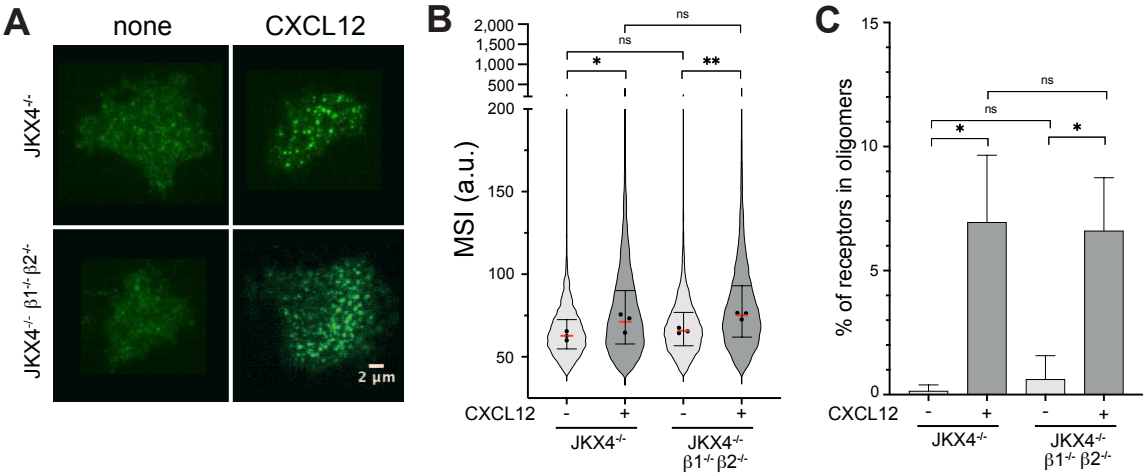


Figure 7. CXCL12-mediated ACKR3 oligomerization is independent of β-arrestin expression. (A) Analysis of CXCL12-mediated ACKR3 nanoclusters in JKX4$^{-/-}$ and JKX4$^{-/-}$β1$^{-/-}$β2$^{-/-}$ cells. Single-particle tracking (SPT) analysis of ACKR3-AcGFP in JKX4$^{-/-}$ and JKX4$^{-/-}$β1$^{-/-}$β2$^{-/-}$ cells on coverslips coated with fibronectin (FN) or FN+CXCL12 (4,529 particles in 69 JKX4$^{-/-}$ cells on FN; 12,221 particles in 68 JKX4$^{-/-}$ cells on FN+CXCL12; 5,350 particles in 69 JKX4$^{-/-}$β1$^{-/-}$β2$^{-/-}$ cells on FN; 13,236 particles in 67 JKX4$^{-/-}$β1$^{-/-}$β2$^{-/-}$ cells on FN+CXCL12) (n = 3). **(B)** Mean spot intensity (MSI) distribution (arbitrary units, a.u.) from individual ACKR3-AcGFP trajectories on unstimulated and CXCL12-stimulated JKX4$^{-/-}$ and JKX4$^{-/-}$β1$^{-/-}$β2$^{-/-}$ transfected cells. The mean of MSI median values from individual experiments is indicated by a horizontal red line; black dots indicate the median MSI values of individual experiments (n = 3; ns = not significant; *P ≤ 0.05, **P ≤ 0.01). **(C)** Frequency of ACKR3-AcGFP receptors organized into oligomers (≥3 receptors per particle) in unstimulated and CXCL12-stimulated JKX4$^{-/-}$ and JKX4$^{-/-}$β1$^{-/-}$β2$^{-/-}$ cells (n = 3; ns = not significant; *P ≤ 0.05).

FIGURE 8

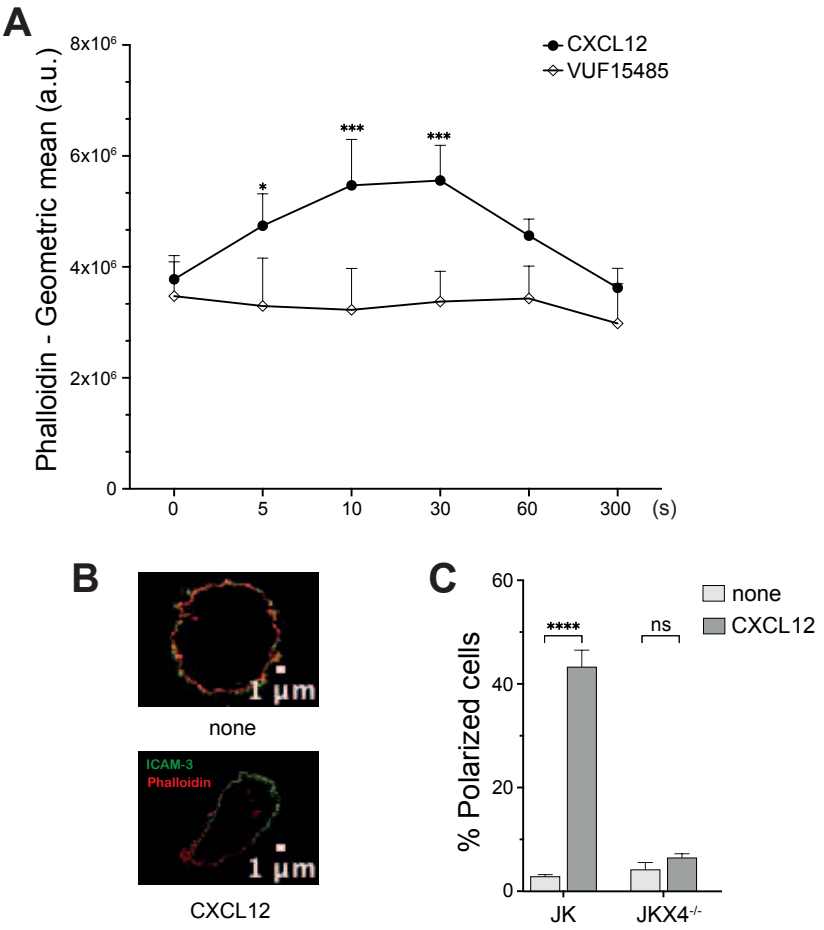


Figure 8. Ligand binding on ACKR3 does not modulate actin cytoskeleton. (A) Actin polymerization in response to CXCL12 or VUF15485, as determined by F-actin (phalloidin-TRITC) staining in JK cells. Statistical significance was calculated for each time point relative to the unstimulated control (mean ± SD; n = 3; *P ≤ 0.05, ***P ≤ 0.001). **(B)** Representative images of a polarized and a non-polarized cell. Red: phalloidin-TRITC, green: anti-ICAM3-Alexa fluor 488. **(C)** Percentage of polarized JK and JKX4$^{-/-}$ cells adhered to fibronectin and treated or not with CXCL12, analyzed by immunostaining with anti-ICAM3-Alexa fluor 488 and phalloidin-TRITC. More than 1,500 cells were analyzed per condition. Data are presented as the percentage of polarized cells (mean ± SD; n = 3; ns = not significant; ****P < 0.0001).

FIGURE 9

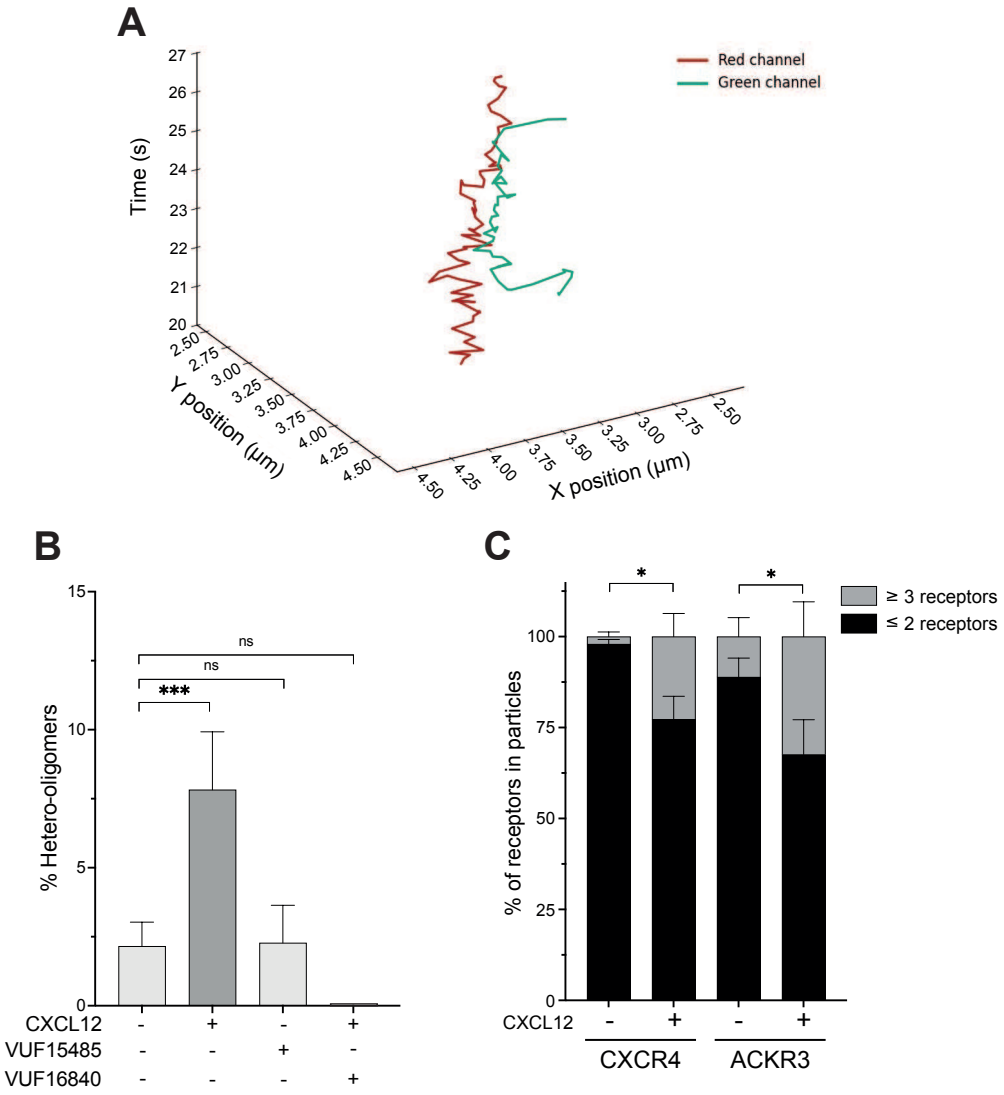


Figure 9. ACKR3 and CXCR4 form dynamic heterocomplexes at the plasma membrane. (A) Representative 3D (X-position/Y position/time) profile of red and green particles from a dual-color TIRF experiment. The trajectories (red and green lines) illustrate the temporal (s) and spatial (µm) overlap of both fluorophores, indicating the formation of heterocomplexes in a subset of frames. **(B)** Percentage of CXCR4/ACKR3 heterocomplexes (≥3 receptors per particle) in unstimulated, CXCL12-, VUF15485- and VUF16860+CXCL12-stimulated knock-in JK cells expressing CXCR4-AcGFP (JKX4-AcGFP-KI) and transfected with ACKR3-SNAP-tag. Single-particle tracking (SPT) analysis was developed using 325 dual trajectories in 134 unstimulated cells, 1,820 in 156 CXCL12 stimulated cells, 107 in 69 VUF15485-stimulated cells. No dual trajectories in 60 VUF16860+CXCL12-stimulated cells were detected. Data represent the mean ± SD (n = 4; ns = not significant; ***P ≤ 0.001). **(C)** Oligomeric organization of CXCR4 and ACKR3 within CXCR4/ACKR3 heterocomplexes. The percentage of each receptor in monomer/dimer states or oligomers (≥3 receptors per particle) is shown for cells as described in (B). Data represent the mean ± SEM (n = 4; *P ≤ 0.05).

FIGURE 10

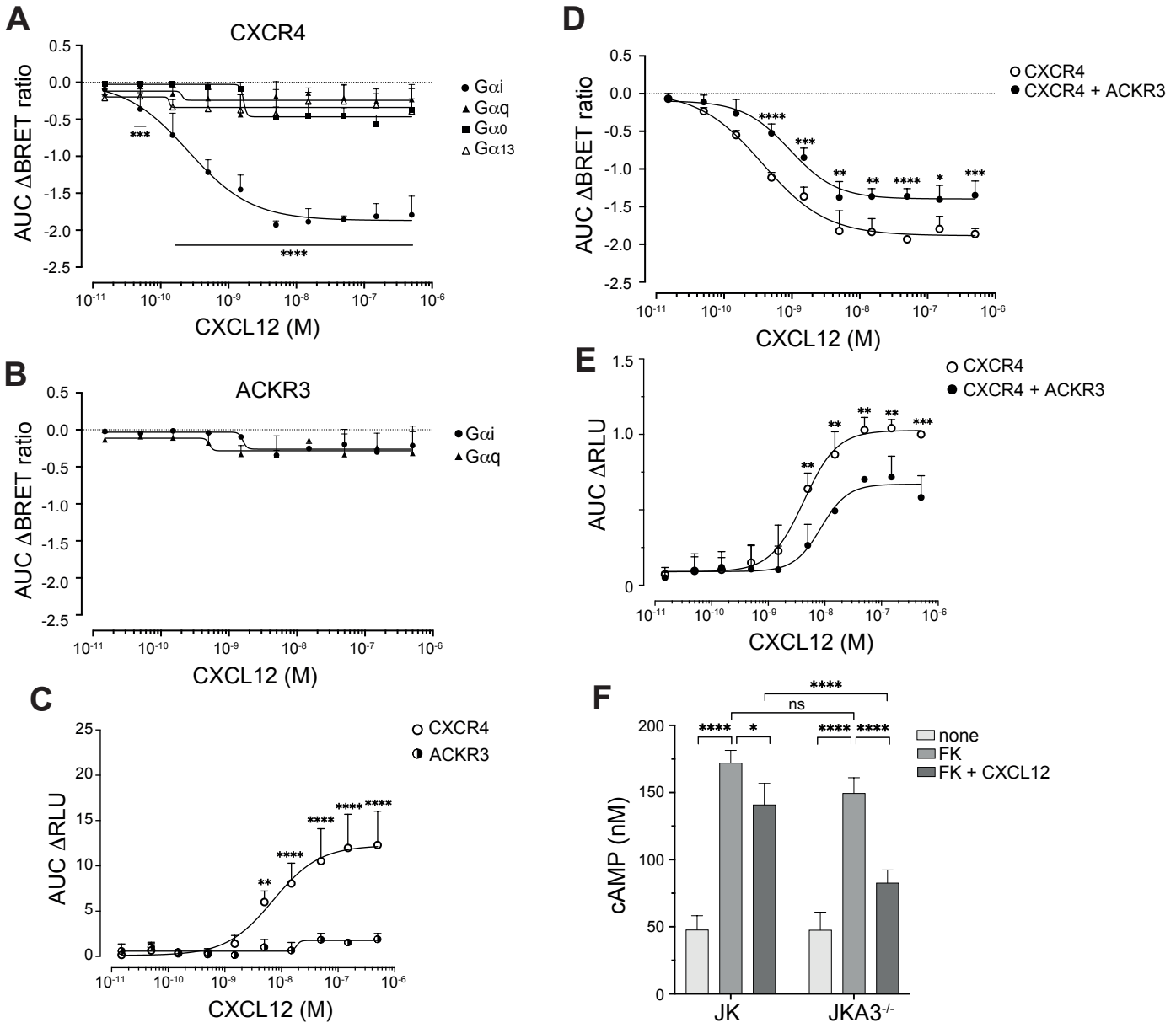


Figure 10. ACKR3 co-expression modulates CXCR4 mediated G-protein activation by CXCL12. (A) HEK-293 cells were transiently co-transfected with pcDNA.3-CXCR4, and a pIRES vector encoding NanoLuc (Nluc)-fused $G\alpha_i$, $G\alpha_o$, $G\alpha_q$, or $G\alpha_{13}$ as well as a Gβ–T2A–cpV–Gγ construct. Cells were stimulated with increasing concentrations of CXCL12. Data represent the mean area under the curve (AUC) ± SD (n = 3; ***P ≤ 0.001; ****P ≤ 0.0001). **(B)** G-protein activation upon addition of increasing concentrations of CXCL12 in HEK-293 cells transiently co-transfected with pcDNA.3-ACKR3, and a pIRES vector encoding Nluc-fused $G\alpha_i$ or $G\alpha_q$ together with a Gβ–T2A–cpV–Gγ construct (n = 3). **(C)** HEK-293 cells were transiently co-transfected with lgBiT-Mini$G\alpha_i$ and either CXCR4-smBiT or ACKR3-smBiT, and then stimulated with increasing concentrations of CXCL12. Data represent the mean AUC ± SD (n = 3; **P ≤ 0.01; ****P ≤ 0.0001). **(D)** HEK-293 cells were transiently co-transfected with pcDNA.3-CXCR4, an empty vector or ACKR3, as well as a pIRES vector encoding Nluc-fused $G\alpha_i$ and a Gβ–T2A–cpV–Gγ construct. Cells were stimulated with increasing concentrations of CXCL12 (n = 3; *P ≤ 0.05; **P ≤ 0.01; ***P ≤ 0.001; ****P ≤ 0.0001). **(E)** HEK-293 cells transiently co-transfected with lgBiT-Mini$G\alpha_i$ and CXCR4-smBiT, in the presence of an empty vector or ACKR3, were treated with increasing amounts of CXCL12. Values were normalized to the highest concentration added to CXCR4 expressing cells. (n = 3; **P ≤ 0.01; ***P ≤ 0.001). **(F)** JK and JKA3$^{-/-}$ cells were either unstimulated or stimulated with CXCL12 (50 nM, 5 min, 37°C), followed by forskolin treatment (10 µM, 10 min, 37°C) or left untreated (none). Cells were lysed, and intracellular cAMP levels were quantified. Data are presented as the mean ± SD (n = 4; ns = not significant; *P ≤ 0.05; ****P ≤ 0.0001).

Supplementary Files

This is a list of supplementary files associated with this preprint. Click to download.

- MOVIES1.avi
- MOVIES10.avi
- MOVIES11.avi
- MOVIES12.avi
- MOVIES13.avi
- MOVIES14.avi
- MOVIES15.avi
- MOVIES16.avi
- MOVIES17.avi
- MOVIES18.avi
- MOVIES19.avi
- MOVIES2.avi
- MOVIES20.avi
- MOVIES21.avi
- MOVIES22.avi
- MOVIES23.avi
- MOVIES24.avi
- MOVIES3.avi
- MOVIES4.avi
- MOVIES5.avi
- MOVIES6.avi
- MOVIES7.avi
- MOVIES8.avi
- MOVIES9.avi
- SupplvideolegendsMsACKR3oligomers.pdf
- SupplementaryFiguresACKR3figurelegends.pdf